

Electrically Controlled Anomalous Hall Effect and Orbital Magnetization in Topological Magnet MnBi_2Te_4

Ruobing Mei,¹ Yi-Fan Zhao,¹ Chong Wang,² Yafei Ren,² Di Xiao,² Cui-Zu Chang,¹ and Chao-Xing Liu¹

¹*Department of Physics, The Pennsylvania State University, University Park, Pennsylvania 16802, USA*

²*Department of Physics, University of Washington, Seattle, Washington, 98195, USA*

In this work, we propose an intrinsic mechanism to understand the even-odd effect, namely the opposite signs of the anomalous Hall resistance and the different shapes of hysteresis loops for even and odd septuple layers (SLs), of MBE-grown MnBi_2Te_4 thin films with electron doping. In particular, we show that the non-zero hysteresis loops in the anomalous Hall and magnetic circular dichroism measurements for even-SLs MnBi_2Te_4 films are originated from two different anti-ferromagnetic (AFM) states with opposite magnetoelectric coefficients that give rise to different energies of zeroth Landau levels of the surface states in this model. The complex form of the anomalous Hall hysteresis loop in even-SLs MnBi_2Te_4 films can be understood from two magnetic transitions, a transition from one AFM state to the other AFM state followed by a second transition to the ferromagnetic state. Our model also provides a microscopic understanding of the electrical switching between two AFM states via the axion electrodynamics in even-SL MnBi_2Te_4 films. We further study orbital magnetization and magnetoelectric coefficient in MnBi_2Te_4 films, and find an even-odd oscillation behavior of the magnetoelectric coefficient.

INTRODUCTION

The recent discovery of MnBi_2Te_4 (MBT) [1–8], a tetradymite-type anti-ferromagnetic compound with topologically non-trivial electronic band structure, provides an excellent platform to explore the interplay between topological physics and magnetism [9, 10]. Exotic magnetic topological phases, including the quantum anomalous Hall (QAH) state [11, 12], axion insulator [11–13] and higher-order Möbius insulator [14], have been theoretically predicted in this compound. For the bulk materials, the A-type of anti-ferromagnetism, namely ferromagnetic coupling in one septuple layer (SL) and anti-ferromagnetic (AFM) coupling between two adjacent SLs, has been unambiguously established through magnetic susceptibility measurements [3, 4] and neutron diffraction experiments [2]. Non-trivial band structure has also been demonstrated through the observation of Dirac surface states with angular-resolved photon emission spectroscopy [3, 15–18], though the existence of magnetic gap of the surface state is still under debate [4, 15, 19, 20]. These experiments confirmed unambiguously the coexistence of magnetic order and topological band structure in bulk MBT.

The situation of the MBT thin films however is subtle. Theoretically, an even-odd effect was predicted for *insulating* MBT films [11–13]. With odd number of SLs, the magnetization on the top and bottom SLs are parallel, leading to a nonzero net magnetization and the QAH state with a quantized Hall resistance. With even number of SLs, the magnetization of the top and bottom SLs are anti-parallel, leading to a zero net magnetization and the axion insulator state [21–36], in which the resistance shows a zero Hall plateau [11, 12]. Later experiments however challenged this scenario through the reflective magnetic circular dichroism (RMCD) and anomalous Hall (AH) measurements in exfoliated MBT flakes

[37–42]. The hysteresis loops from both measurements are not synchronized. Specifically, with the odd number of SLs, RMCD signals exhibit a clear hysteresis loop whereas the AH hysteresis loop is almost invisible. With even number of SLs, a small RMCD signal around zero external field was reported, whereas a clear anomalous Hall resistance hysteresis loop is found. These experimental findings indicate the complexity of real materials where the complex chemical and magnetic environments that depend on individual sample qualities might play a role.

More recently, another type of even-odd effect was found in the *metallic* MBT films grown by molecular beam epitaxy (MBE) method in the electron doping regime [43]. Although the metallic samples with both even and odd SLs show hysteresis loops in AH resistance, the shapes of the loops are clearly distinct. In both cases, the AH resistance hysteresis loops can be decomposed into two AH components. One component behaves the same for the even and odd SLs, which is a trivial component with a smaller coercive field from the minor Mn-doped Bi_2Te_3 phase. The other AH component is expected to be from the dominant MBT phase and shows interesting even-odd effect: (1) The signs of AH resistance at zero magnetic field are opposite for even and odd SLs; (2) For even SLs, the AH sign reverses twice around the spin-flop transition between the AFM state and canted AFM state, as shown in Fig. S1(a), which reproduces the transport data in Fig. 3g of Ref. [43] (one can also find similar data in Fig. 4e of Ref. [37] and Fig. 2b of Ref. [39] for even-SL MBT films), while no such behavior occurs for odd SLs. We notice that such patterns have also been observed in even SLs of MBT films that are fabricated by flux method followed by mechanical exfoliation [37, 39, 44]. In Ref. [37], the opposite AH signs of MBT films with even and odd SLs were attributed to the competition between intrinsic (Berry curvature contribution) and extrinsic (impurity

scattering contribution) AH effects [45]. However, as the samples prepared in different approaches (MBE or mechanical exfoliation) have very different disorder levels, this motivates us to explore intrinsic mechanism for this even-odd effect.

In this work, we provide a theoretical understanding of the AH hysteresis loop observed in MBT films based on a two-surface-state model and a four-band thin film model. We show that for electron doping case, the intrinsic AH signs in even and odd SLs are opposite. In particular, with even SLs, we argue that there are two AFM states (see Fig. S1(b)) that are degenerate in the presence of inversion symmetry. The inversion symmetry breaking from the substrate and external gates splits these two AFM states, leading to the AH hysteresis loop in even SL MBT films. Around the spin-flop transition, there are actually two magnetic transitions: the system transits from one AFM state to the other AFM state first and then to the ferromagnetic (FM) state, causing the double sign changes in the AH response (see Fig. S1(a)). In contrast, with hole doping, we show that the AH signs in even and odd SLs are the same.

We then turn to the orbital magnetization. In ferromagnetic materials, local magnetic moments usually come from electron spin, which are much larger than orbital magnetic moments that originate from electron's orbital motion [46]. Orbital ferromagnetism in twisted bilayer graphene is an exempt due to the lack of spin local magnetic moments of carbon atoms [47–49]. In A-type AFM materials, such as MBT, the cancellation of spin magnetization in adjacent SLs makes the orbital magnetization important in the magnetoelectric properties of the materials. We calculate the layer number dependence of orbital magnetization in MBT films and find that the orbital magnetization in even SLs has a linear dependence on the electric field, while it remains a constant under varying electric field in odd SLs. We thus can extract the magnetoelectric coefficient, which approaches the bulk value determined by the axion parameter as the layer thickness increases for even SLs and stays zero for odd SLs, revealing an even-odd oscillation behavior. We also clarify the relation and distinction between the axion parameter that features the axion insulator phase and magnetoelectric coefficient that characterizes the magnetoelectric response and can be quantized for topological magnetoelectric effect.

EVEN-ODD EFFECT OF HYSTERESIS LOOP IN MBT FILMS

We start from a symmetry consideration of the AFM states in even SL MBT films. For even SLs, there are two possible AFM configurations, labelled as AFM1 and AFM2, and the magnetization in each SL for AFM1 is opposite to that for AFM2, as shown in Fig. S1(b). Without any external fields, both AFM ground states spontaneously break inversion \hat{I} or time reversal symmetry

\hat{T} . AFM1 is related to AFM2 by either \hat{I} or \hat{T} operation and thus they have the same ground state energy. Similarly, in the presence of an external magnetic field (electric field), these two AFM ground states are still energetically degenerate since they can be related to each other by \hat{I} (\hat{T}). Breaking both \hat{I} and \hat{T} explicitly is essential to energetically distinguish these two AFM states. In experiments, the degeneracy can be lifted in the presence of both magnetic field and effective electric field from the asymmetric substrates or electric gates [41, 44].

To make the above argument more concrete, let us consider a simple model for the MBT films with two surface states, and the corresponding Hamiltonian can be expressed as

$$H = H_M + H_e + H_{e-M}, \quad (1)$$

where H_M is the magnetization part, H_e is the electron part and H_{e-M} is the coupling between electrons and magnetization. Specifically,

$$H_M = J\mathbf{m}_{s1} \cdot \mathbf{m}_{s2} - M_s \mathbf{B} \cdot (\mathbf{m}_{s1} + \mathbf{m}_{s2}) - \frac{K}{2}(m_{s1,z}^2 + m_{s2,z}^2), \quad (2)$$

[39, 50, 51] where $\mathbf{m}_{si} = (\sin\theta_i \cos\phi_i, \sin\theta_i \sin\phi_i, \cos\phi_i)$ is the magnetization vector with polar and azimuthal angles θ and ϕ , the index $i = 1, 2$ labels the magnetization at the top and bottom surfaces, M_s is the saturation magnetization, J labels the effective exchange coupling between magnetizations at two surfaces ($J > 0$ for AFM and $J < 0$ for FM), \mathbf{B} is the external magnetic field and K is easy-axis anisotropy. Here we have absorbed the magnitude of magnetization into the definition of the parameters J , K and M_s , so \mathbf{m}_{si} is a unit vector ($|\mathbf{m}_{si}| = 1$). For H_e , we consider two-surface-state model with the electron Hamiltonian

$$H_e = v_f((k_x + \frac{e}{\hbar}A_x)\sigma_y - (k_y + \frac{e}{\hbar}A_y)\sigma_x)\tau_z + V_0\tau_z/2, \quad (3)$$

where σ and τ are Pauli matrices in the spin and layer sub-space, v_f is the Fermi velocity, V_0 is the asymmetric potential between two surfaces and the Landau gauge is chosen as $\mathbf{A} = (0, A_y, 0) = (0, Bx, 0)$ for the out-of-plane magnetic field $\mathbf{B} = (0, 0, B)$. The electron-magnetization coupling Hamiltonian depends on magnetic configurations, and takes the form

$$H_{e-M} = gM_s \begin{pmatrix} m_{s1,z}\sigma_z & 0 \\ 0 & m_{s2,z}\sigma_z \end{pmatrix} \quad (4)$$

where g is the exchange coupling coefficient between electrons and magnetic moments and the two blocks of the above Hamiltonian are for two surfaces. Here the exchange coupling of in-plane magnetization is dropped because it only shifts the locations of surface Dirac point and can be generally absorbed into the gauge potential \mathbf{A} . The directly Zeeman coupling between electron spin and external magnetic field is dropped as it is much smaller than the exchange coupling at the low magnetic field limit. The magnetic simulation in Ref. [13] and

[39] suggests that the ground state of H_M is given by the out-of-plane AFM configurations with $\mathbf{m}_{s1} = (0, 0, \pm 1)$ and $\mathbf{m}_{s2} = -\mathbf{m}_{s1}$ at zero or low external magnetic fields, which just corresponds to the AFM1 and AFM2 shown in Fig. S1(b). Thus, the magnetization energy for these two AFM states is $E_M = -J - K$. The energy of AFM states is independent of magnetic field B due to the zero total magnetization $\mathbf{m}_{s1} + \mathbf{m}_{s2} = 0$. On the other hand, the FM state has the magnetization energy $E_M = J - K \pm 2M_s B$, where \pm selects the FM state with magnetization vectors aligned with B as the favored configuration. Thus, for $J > 0$, the AFM states have lower energy while the FM state can be energetically favored at a large B . To distinguish the ground state energy for two AFM states, we need to further include the electron energy from $H_e + H_{e-M}$, which involves the Landau level (LL) spectrum in the presence of magnetic fields (see Appendix Sec.I.A). For Dirac surface states, besides the normal LLs, given by $\varepsilon_{\mu,\nu}^N = \mu\sqrt{2v_f^2 N/l_c^2 + (gM_s)^2} + \nu V_0/2$, where $\mu, \nu = \pm 1$, $N = 1, 2, \dots$ representing the N th LL and $l_c = \sqrt{\frac{\hbar}{eB}}$ is the magnetic length, there are additional zeroth LLs (zLLs), given by $\varepsilon_{1,\lambda}^0 = \lambda V_0/2 + \lambda gM_s$ for the AFM1 state and $\varepsilon_{2,\lambda}^0 = \lambda V_0/2 - \lambda gM_s$ for the AFM2 state under positive magnetic field, where $\lambda = +$ ($\lambda = -$) corresponds to the zLL on the top (bottom) surface. We first notice that all the higher LLs ε^N ($N > 0$) of these two surface states are equivalent for the two AFM configurations, even in the presence of both electric and magnetic fields. Thus, all the energy difference between two AFM states comes from the zLLs. The energies of the zLLs depend on the signs of the magnetic gaps (the sign of g and $m_{si,z}$ in H_{e-M}). When $g > 0$, for the AFM1 (AFM2) configuration, the zLL for the top surface state with $\lambda = +$ has the energy of the conduction band bottom (valence band top) while that for the bottom surface state with $\lambda = -$ is at the valence band top (conduction band bottom), as shown in Fig. S1(c). At zero electric field $V_0 = 0$, the occupied zLL has the same energy for two AFM configurations $\varepsilon_{1,-}^0 = \varepsilon_{2,+}^0 = -gM_s$, but this degeneracy will be broken by an external electric field, which shifts the energies $\varepsilon_{1,-}^0$ and $\varepsilon_{2,+}^0$ oppositely. As a result, for $V_0 > 0$, the occupied zLL of AFM1 decreases in energy ($\varepsilon_{1,-}^0 = -V_0/2 - gM_s$) while that of AFM2 increases ($\varepsilon_{2,+}^0 = V_0/2 - gM_s$) (Fig. S1(d)), and the energy difference between them is $\Delta\varepsilon = \varepsilon_{1,-}^0 - \varepsilon_{2,+}^0 = -V_0 < 0$. Therefore, AFM1 is energetically favored for $V_0 > 0$ that corresponds to the anti-parallel alignment of external electric and magnetic fields (we choose $V_0 = -eEL$ with E representing electric field and L the film thickness). For $V_0 < 0$ (parallel alignment of electric and magnetic fields), AFM2 has a lower ground state energy than AFM1 as $\Delta\varepsilon = -V_0 > 0$. Therefore, we have shown microscopically the energy difference between two AFM states arises from the energy shift of zeroth LLs of Dirac surface states under electric fields.

After identifying the lower-energy AFM configuration

under both external magnetic and electric fields, we next study the sign of anomalous Hall (AH) conductance for the two-surface-state model of the MBT films. According to Fig. 3 in Ref. [43], the MBT samples are heavily electron-doped so that the ordinary Hall resistance shows a negative slope. For odd SL MBT films, when reducing magnetic fields from a large value to zero, the zero field AH resistance shares the same sign as the ordinary Hall resistance without any sign change. We find that only the Landau level spectrum for $g > 0$ is consistent with the above experimental observations within our current definition of the parameters, and thus we can fix the exchange coupling sign as positive (see Appendix Sec.I.B for more details). In contrast, the signs between zero field AH resistance and ordinary Hall resistance for even SL MBT films are opposite. The sign of AH for each band is fixed by the magnetization vectors $m_{s1,z}$ and $m_{s2,z}$. We first consider the odd SL with $m_{s1,z} = m_{s2,z} = 1$, which are in alignment with a positive magnetic field. To be consistent with the experiments, we determine that the valence bands of both surfaces contribute negative AH sign while the conduction bands contribute positive AH sign (see Appendix Fig. S1(b)). For even SL, the AH signs of bands are reversed for the surface whose magnetization is flipped compared to that of odd SL. Therefore, the valence band of the top (bottom) surface should contribute a positive (negative) sign to the AH conductance for AFM1, and vice versa for AFM2, as illustrated in Fig. S1(c), where blue and red stand for positive and negative AH signs, respectively. When the Fermi level is within the magnetic gap (i.e. charge neutral point), the valence bands of the top and bottom surfaces give exact opposite contributions, which leads to zero overall AH conductance. For the system with $E > 0$ ($V_0 < 0$) at electron doping, the favored AFM configuration is AFM2, so the conduction band of the top surface appears near the Fermi energy and contributes a positive sign to the overall AH conductance (Fig. S1(e)). When $E < 0$ ($V_0 > 0$), the favored AFM configuration is AFM1, which also exhibits positive AH conductance at electron doping (Fig. S1(d)). Therefore, at electron doping, the energetically favored AFM state of even-SLs MBT films always possesses a positive sign of the AH conductance under a positive magnetic field, regardless of the direction of the electric field. Under negative external magnetic field, similar analysis suggests that the odd SL MBT film displays positive AH, while the even SL shows negative AH. We conclude that the odd and even SL films will always have opposite AH signs at electron doping, which is independent of the alignment between electric and magnetic fields. These results explain the observations of the even-odd AH effect in both exfoliated and MBE-grown samples, where the systems are electron doped.

The situation is dramatically changed for the hole doping. For $B > 0$ and $E > 0$, the Fermi level now crosses the valence band of the bottom surface in AFM2, so that all the occupied states contribute a negative AH conduc-

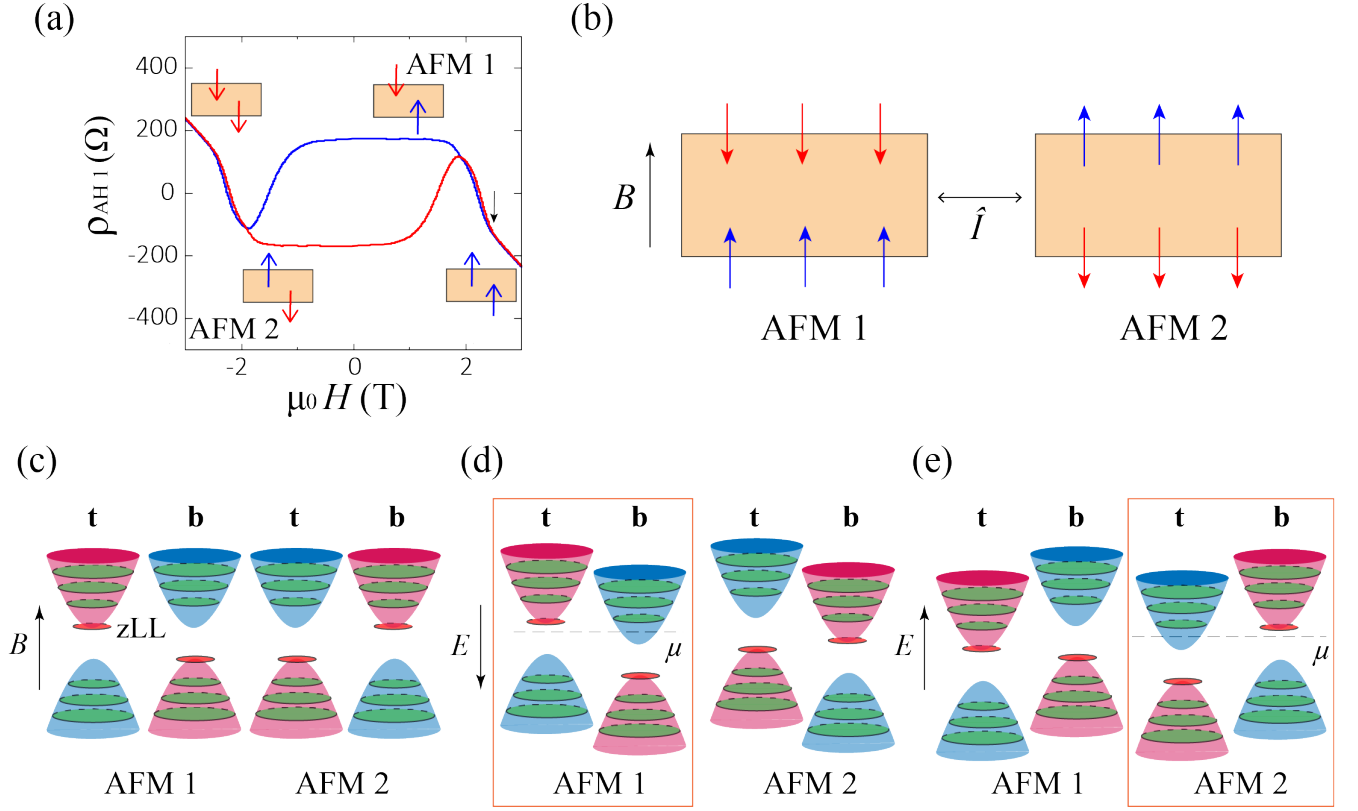


FIG. 1. (a) Experimental measurement of AH resistance ρ_{yx} as a function of magnetic field $\mu_0 H$ in a 2 SL MBT film. The spin-flop field is around 2.3 T, indicated by the black arrow. Here only the contribution to the Hall resistance from the intrinsic AH effect in MBT is included while other contributions, e.g. the AH contributions from Mn doped $(\text{Bi,Sb})_2\text{Te}_3$ and ordinary Hall effect, have been excluded. The intrinsic AH contribution for other even SL MBT films is similar to that of 2S SL MBT films. See Ref. [43] for more details. (b) Magnetization configurations of even SL MBT films. Under an external magnetic field, there are two possible AFM configurations related by inversion symmetry, which are energetically equivalent. (c) Illustration of the two-surface state model for $g > 0$ and $B > 0$, where "t" and "b" stand for top and bottom surfaces, respectively. Each band is labeled with blue or red color, which represents positive or negative AH sign. The zeroth Landau levels are shown in red and the other Landau levels are shown in green. (d) When an electric field E is present, the top and bottom surfaces split in energies. For a negative E ($V_0 > 0$), the occupied zLL in AFM1 is lower in energy than that in AFM2, and therefore, AFM1 becomes the favored configuration. At electron doping, the conduction band of the bottom surface contributes positive AH sign (blue color). (e) For a positive E ($V_0 < 0$), AFM2 is the favored state also with positive AH sign at electron doping.

tance, which is the same sign of the AH conductance in odd SL. Similar situation occurs for $B > 0$ and $E < 0$. Therefore, the odd SL and even SL both exhibit negative (positive) AH sign under positive (negative) magnetic field, again regardless of the electric field direction. This is consistent with the experiment in Ref. [44], where the 5 SL sample was shown to exhibit negative AH at both electron and hole doping, while the 6 SL sample displays negative and positive AH resistance at hole and electron doping, respectively.

To buttress our arguments, we also investigate a thin film model which includes both surface and bulk states, and perform numerical calculations for the energy of zLLs and the corresponding AH conductivity for 2 SL MBT films (see Appendix Sec.I.B). Although we only show the results for 2 SL MBT film for simplicity, the conclusion

can be applied to thicker even SL films. For 2 SL MBT, there are four possible AFM and FM configurations as shown in Fig. S2(a). We denote the ground state energy density of the AFM1 and AFM2 configurations as ε_1 and ε_2 , respectively, and calculate the energy density difference $\Delta\varepsilon = \varepsilon_1 - \varepsilon_2$ as a function of the magnetic field B and the asymmetric potential $V_0 = -eEL$ induced by the out-of-plane electric fields E with L being the film thickness (Fig. S2(b)). As expected, for $\mathbf{B} \cdot \mathbf{E} < 0$, we find $\Delta\varepsilon < 0$ so that the AFM1 configuration is energetically favored, while for $\mathbf{B} \cdot \mathbf{E} > 0$, $\Delta\varepsilon > 0$ and the AFM2 configuration is preferred. We then compare the Hall conductivity in 2 SL and 3 SL MBT films at both electron and hole doping with carrier density $n = \pm 2 \times 10^{-12} \text{cm}^{-2}$ for a positive magnetic field, as shown in Fig. S2(c). For 3-SL MBT films, the top and

bottom SLs have parallel magnetization, and the middle SL has opposite magnetization due to AFM (see Appendix Fig. S2(a)). At the asymmetric potential $V_0 = 0$, the 2 SL MBT presents zero Hall conductance as the top and bottom surface states cancel out their contributions, while the 3 SL MBT has a negative AH conductance for both electron and hole-doping. When V_0 is nonzero, the electric field can induce a nonzero AH response in 2 SL, which is positive (negative) in the electron-doped (hole-doped) regime. On the other hand, the doping does not have any influence on the sign of AH conductance in 3 SL MBT, which only weakly varies with the electric fields. In summary, at electron doping, the 2 SL and 3 SL MBT show opposite AH signs, while at hole doping, they have the same sign of AH conductance, which is consistent with the analysis based on the two-surface-state model.

We further investigate the hysteresis loop for even SL MBT films. In Fig. S2(d), we show the Hall conductivity σ_{xy} for all the AFM and FM states at electron density $n = 2 \times 10^{-12} \text{cm}^{-2}$ for $V_0 > 0$ and sketch the expected favored states at different B by the red line. To determine the favored state between FM and AFM states, we refer to the magnetization energy E_M . We estimate the spin-flop transition occurring around the field $B_c^\pm = \pm B_c \approx \pm J/M_s$ (As the in-plane magnetization is not included here, we did not study the canted AFM phase during the spin-flop transition), and for $|B| > B_c$, the FM states have the lower magnetization energy and the magnetization of both SLs tends to align with the magnetic field, which means that FM1 is favored at $B > B_c^+$ and FM2 is favored at $B < B_c^-$. For $|B| < B_c$, the AFM states have lower energy, and at $0 < B < B_c^+$ AFM1 is the favored state, while at $B_c^- < B < 0$ AFM2 is the favored state for $V_0 > 0$, as demonstrated previously. As shown in Fig. S1(a), the typical value of the spin-flop field B_c for 2 SL MBT film in the experiment is around 2.3 T [43]. When the magnetic field is swept from positive to negative, the favored state for 2-SL films goes through FM 1 \rightarrow AFM 1 \rightarrow AFM 2 \rightarrow FM 2 and correspondingly the sign of Hall conductivity σ_{xy} varies as $- \rightarrow + \rightarrow - \rightarrow +$, as shown by the red lines in Fig. S2(d). Since the phase transition between the AFM1 and AFM2 configurations around $B \approx 0$ is of the first order, a hysteresis loop can form at small magnetic fields before the spin-flop transition that occurs at larger magnetic fields, as shown by the black dashed lines in Fig. S2(d), which give rise to the form of the AH hysteresis loop observed in experiments in Fig. S1(a). The double sign changes of the observed hysteresis loop in experiments can be understood as a two-step phase transition: the first-step transition between two AFM states followed by the second-step transition between the AFM and FM states.

The dependence of the ground state energy of AFM configurations on electric fields implies the possibility of electrical control of AH near the AFM states transition point. For a positive magnetic field, the Hall conductance of the AFM1 (AFM2) configuration is positive (negative)

for $V_0 > 0$, negative (positive) for $V_0 < 0$ and zero at $V_0 = 0$. If we sweep the electric field from positive to negative as illustrated by the blue curve in Fig. S2(e), the favored configuration changes from AFM 1 to AFM 2 according to Fig. S2(b), so the Hall conductance of the favored state should always be positive. However, due to hysteresis, the system stays in AFM 1 for a short moment after the electric field flips before transiting to AFM 2. As a result, the Hall conductivity first changes from positive to negative momentarily then back to positive, so the sign change in AH due to the hysteresis loop is an indicator of the transition between two AFM states. This physical picture of electric control of Hall conductance potentially corresponds to the recent experimental observations of the switching of AH sign by scanning the electric field back and forth [44]. This observation was interpreted as the consequence of the phenomenological axion electrodynamics while our understanding based on the zLLs is equivalent to that but provides a microscopic physical picture.

ORBITAL MAGNETIZATION AND MAGNETOELECTRIC EFFECT IN MBT FILMS

In this section, we will discuss an alternative view point of the magnetic transition between different AFM states based on the orbital magnetization created by magnetoelectric effect in the MBT films. Magnetic moments have two origins: spin and orbital moment. Normally, magnetic moments from spin is much larger than orbital moments. For odd-SL MBT films, there is an uncompensated net spin magnetization, and thus the orbital magnetization is negligible. For even SLs, however, the spin magnetization cancels out in the AFM configuration, and thus the orbital magnetization can play a role. The even-SLs MBT films are expected to host the magnetoelectric effect, which means that an electric field can create a magnetization, given by $\mathbf{M} = \alpha \mathbf{E}$, where the α is the magnetoelectric coefficient. The magnetoelectric effect has been previously studied in 2D magnetic materials [52, 53]. As studied below, in the MBT films, this electric field induced orbital magnetization depends on the AFM configurations and has opposite sign between AFM1 and AFM2, so that it can provide an alternating understanding on different energies between two AFM configurations under an external magnetic field.

The orbital magnetization usually contains two parts, a trivial part and a topological part [54–57],

$$\begin{aligned} m_{\text{total}} &= m_{\text{trivial}} + m_{\text{topological}}, \\ m_{\text{trivial}} &= -\frac{ie}{2\hbar} \langle \nabla_k u | \times [H(k) - \epsilon(k)] | \nabla_k u \rangle, \\ m_{\text{topological}} &= -\frac{ie}{2\hbar} \langle \nabla_k u | \times 2[\epsilon(k) - \mu] | \nabla_k u \rangle, \end{aligned} \quad (5)$$

where $\epsilon(k)$ and $|u\rangle$ are the eigenvalues and eigenstates of the Hamiltonian $H(k) = H_e + H_{e-M}$ of the system, and μ is the Fermi energy. Intuitively, the trivial part

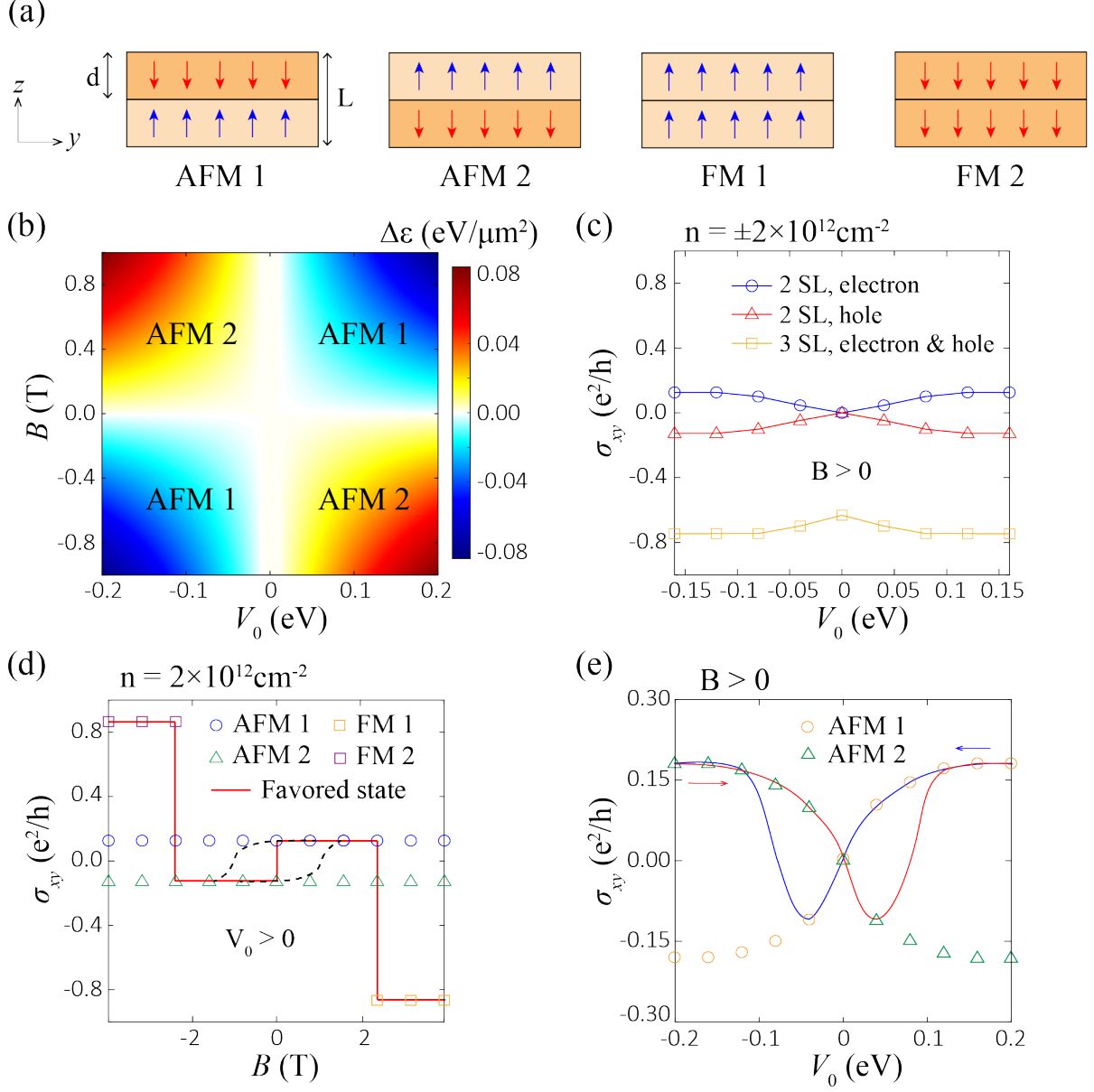


FIG. 2. (a) Illustration of thin film model for 2 SL MBT films. Each SL has a thickness of d . For AFM states, the adjacent layers have anti-parallel magnetization and for FM states the two layers have parallel magnetization. (b) The energy density difference between AFM1 and AFM2 $\Delta\epsilon = \epsilon_1 - \epsilon_2$ as a function of asymmetric potential V_0 and magnetic field B at electron density $n = 2 \times 10^{12} \text{cm}^{-2}$. When $B \cdot V_0 > 0$, $\Delta\epsilon < 0$, and thus AFM1 is the favored state; when $B \cdot V_0 < 0$, $\Delta\epsilon > 0$, so AFM2 becomes the favored configuration. (c) Numerically calculated Hall conductivity σ_{xy} as a function of V_0 for favored 2 SL and 3 SL samples at electron and hole doping under positive B with carrier density $n = \pm 2 \times 10^{12} \text{cm}^{-2}$. The 2 SL with electron doping exhibits opposite AH sign compared to both the 2 SL with hole doping and 3 SL. (d) Hall conductivity σ_{xy} as a function of B at electron density $n = 2 \times 10^{12} \text{cm}^{-2}$ for positive V_0 . The red line is the expected favored state at different B . The spin-flop transition field is around 2.3 T for even MBT films. The hysteresis loop is expected around $B = 0$ T before the spin-flop transition, as illustrated by the dashed black lines. (e) Electric control of Hall conductivity for 2 SL. The yellow circles and green triangles stand for the Hall conductivity for AFM1 and AFM2 respectively. AFM1 and AFM2 are the favored states for $V_0 > 0$ and $V_0 < 0$, and they both display zero AH conductivity at zero V_0 . As V_0 sweeps from positive to negative (blue line), the Hall conductivity experiences a sign change as AFM1 persists through the small negative V_0 until AFM2 takes over.

comes from the self rotation of a wave packet around its center of mass, and the topological part originates from the center of mass motion under the presence of boundary potentials, which relates to the Berry curvature.

Figure S3(a)-(d) show the orbital magnetic moment as a function of asymmetric potential V_0 for 2-5 SL in the thin film model at chemical potential $\mu = 0$. Figure S3(a), (c) show the orbital magnetic moment for the 2 and 4 SLs in AFM1 configuration, which is zero for $V_0 = 0$ and linearly increases with V_0 . This orbital magnetic moment is thus induced by z-direction electric field corresponding to the magnetoelectric effect. The signs of all the magnetic moment components reverse for AFM2. In the presence of external magnetic fields, the electric-field-induced orbital magnetization can lead to the energy difference $\Delta\varepsilon = \varepsilon_{AFM1} - \varepsilon_{AFM2} = \mathbf{M}_{orb,1} \cdot \mathbf{B} - \mathbf{M}_{orb,2} \cdot \mathbf{B}$ between two AFM states, where $\mathbf{M}_{orb,1}$ and $\mathbf{M}_{orb,2}$ are the orbital magnetization of AFM1 and AFM2, respectively. Our calculations show that a negative electric field, namely $V_0 > 0$, can induce a negative (positive) total orbital magnetization $\mathbf{M}_{orb,1} = -M_0\hat{z}$ ($\mathbf{M}_{orb,2} = M_0\hat{z}$) for the AFM1 (AFM2) configuration, where M_0 is a positive number and \hat{z} is the unit vector along z axis, so $\Delta\varepsilon = -2M_0B < 0$ at positive magnetic field B , which means that AFM1 is the favored configuration, and $\Delta\varepsilon = 2M_0B > 0$ at negative magnetic field $-B$, for which AFM2 is favored. Therefore, we arrive at the same conclusion as that from the perspective of zLLs, namely AFM1 is the favored state for $\mathbf{B} \cdot \mathbf{E} < 0$ and vice versa.

We notice that in even SLs, both trivial and topological parts have non-zero slopes while they remain constants in odd SLs, which is consistent with the results for two-surface state model (see Appendix Sec.III). We estimate the magnitude of the calculated orbital magnetization and compare it to the Bohr magneton. Using Bohr magneton $\mu_B = \frac{e\hbar}{2m_e} = \frac{2\pi e}{h} R_y a_0^2$ with Rydberg constant $R_y \simeq 13.6\text{eV}$ and Bohr radius $a_0 \simeq 5.29 \times 10^{-11}\text{m}$, we derive $\frac{e}{h} = \frac{\mu_B}{2\pi a_0^2 R_y} \simeq 4.18\mu_B/(\text{nm}^2 \cdot \text{eV})$. For an electric field strength $E = 0.1\text{V/nm}$, the orbital magnetic moment in the even SL is about $10^{-1} \frac{e}{h} \cdot \text{eV} \sim 0.4\mu_B/\text{nm}^2$. The Mn ions have a magnetic moment of $\sim 5\mu_B$ and the in-plane lattice constant of MBT is $a \simeq 0.43\text{nm}$ [2], so the spin magnetization is around $27\mu_B/\text{nm}^2$, and hence the orbital magnetization is approximately two orders smaller than the spin magnetization, which thus can only play a role when spin magnetization is cancelled, e.g. AFM configuration.

We further extract the magnetoelectric coefficient α from the orbital magnetization [58–60], defined by $\mathbf{M} = \alpha\mathbf{E}$. As shown in Fig. S3(e), we find that for even SLs, the trivial part of α goes to zero and the topological part approaches quantized value $e^2/2h$ as the layer number increases at $\mu = 0$. On the other hand, the odd SLs always exhibit zero α although the orbital magnetization is nonzero. Thus, there exists an even-odd effect of magnetoelectric coefficient α , which oscillates between zero and nonzero as the layer number of MBT films alternates between odd and even in Fig. S3(e). The behaviors of α

for a nonzero chemical potential μ are shown in Appendix Sec.III.

We should distinguish magnetoelectric coefficient α from the axion parameter θ , a three-dimensional (3D) bulk quantity that characterizes axion electrodynamics in topological insulators (TIs) [13, 35, 58–62]. In the field theory description of 3D TIs, a topological θ term $\theta e^2 \mathbf{E} \cdot \mathbf{B}/2\pi h$ is added into the ordinary Maxwell electromagnetic Lagrangian, in which \mathbf{E} and \mathbf{B} are the conventional electric and magnetic fields inside an insulator, and θ is a pseudo-scalar and called the axion parameter. When time reversal symmetry is present, θ can only takes two quantized values 0 and π , corresponding to trivial insulators and TIs, respectively [62]. The axion parameter θ can be directly connected to magnetoelectric coefficient α (an experimental observable) as $\alpha = \theta e^2/2\pi h$ when all the surface states of 3D TIs are gapped. This can only be achieved in magnetic TIs with the AFM alignment of magnetization between top and bottoms surfaces, so that all surface states are gapped out. For the MBT films, this corresponds to even SLs in the large thickness limit, and the magnetoelectric coefficient α value approaches $e^2/2h$ (Fig. S3(e)) as $\theta = \pi$ in bulk MBT, namely the topological magnetoelectric effect for the axion insulator phase. On the other hand, for the thick MBT films with odd SLs (parallel magnetization alignment between two surfaces), our calculations suggest magnetoelectric coefficient α is zero, different from the bulk axion parameter value ($\theta = \pi$). As its bulk θ value is quantized to be π , such phase in the 3D limit is previously studied as the axion insulators with higher-order topology [23, 24, 34, 63–66], in which metallic modes exist at the hinges of finite samples.

Our results also suggest that even though the spin magnetization is zero in even SLs, the orbital magnetization can have an impact in the magnetization measurements, e.g. the magnetic circular dichroism (MCD) experiment [42]. In fact, the early RMCD experiments show a non-zero hysteresis loop around small magnetic fields, which was assumed to come from magnetic domains/disorders in the system [39, 40]. Our studies of the orbital magnetization here provides an intrinsic mechanism for these observations. A decent RMCD signal may also come from the p-d transition of magnetic ions while the orbital magnetization discussed here may be more sensitive to a small photon energy that matches the topological gap. Thus, examining the frequency dependence of RMCD may provide information of the origins of RMCD signals. We also notice that a recent work suggests the RMCD signals for even-SL MBT can exist as the reflections from the top and bottom surface states are not identical, leading to a finite Kerr rotation at a certain photon wavelength in the Kerr experiment configuration, while the transmission part of the MCD (Faraday rotation) remains zero [67]. Therefore, while the RMCD signals may have the contributions from both mechanisms, the transmission MCD signals will be dominated by orbital magnetization discussed here. Electric control of the orbital magne-

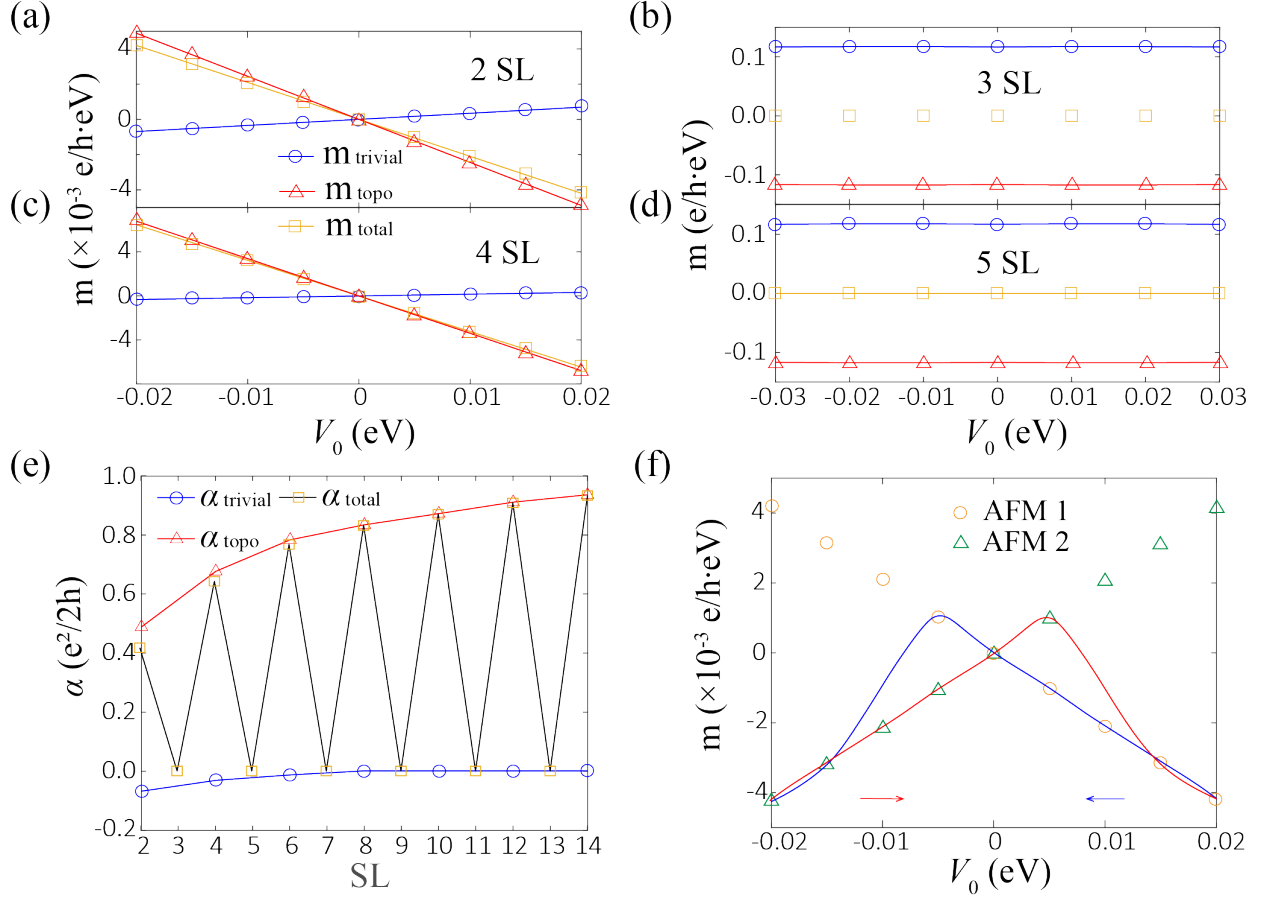


FIG. 3. Calculated orbital magnetic moment m as a function of V_0 for (a) 2SL, (b) 3SL, (c) 4SL and (d) 5SL in the thin film model for chemical potential $\mu = 0$. The blue, red and yellow lines are for trivial, topological and total magnetic moment, respectively. In even SLs, m displays non-zero slope versus V_0 , while in odd SLs, m is a constant under varying V_0 . (e) The trivial and topological part of α and total α as a function of SL number. (f) Illustration of the electric control of orbital magnetic moment in even SL MBT.

tization in even SL can also be realized by measuring the MCD signals while sweeping the electric field, as illustrated in Fig. S3(f). Following the blue curve, at positive V_0 , AFM1 is the favored configuration with negative orbital magnetization, and the magnetization vanishes at $V_0 = 0$. As V_0 turns to a small negative value, the system remains in the AFM1 with the positive orbital magnetization as the AFM1-AFM2 transition is of the first order, giving rise to the hysteresis loop, similar to the Hall resistance hysteresis loop discussed in Fig. S2(e). The transition from AFM1 to AFM2 is expected to occur at a certain negative value of V_0 , and the orbital magnetization changes to negative after this value of V_0 . Therefore, the orbital magnetization is expected to vary from negative to positive then back to negative as the electric potential V_0 sweeps from positive to negative.

CONCLUSION AND DISCUSSION

In summary, we use a two-surface-state model and a thin-film model to study the MBT films, and demonstrate that the presence of electric and magnetic fields can select a favored AFM configuration in even SL through the effect of zLLs, which leads to a nonzero AH response and orbital magnetization in the system. Our results provide a possible explanation for the hysteresis loops of even and odd SL MBT observed in experiments. For the real experimental samples, disorders and magnetic domains are inevitable. For example, antiferromagnetic domain walls have been imaged in MBT via cryogenic magnetic force microscopy [68]. Thus, the transition between two AFM states discussed here corresponds to the enlargement and shrinkage of two opposite AFM domains in real samples. Furthermore, bulk states, in addition to surface states, may also play a role due to

the chemical potential inhomogeneity. Consequently, we expect more complicated behaviors due to the interplay between intrinsic and extrinsic mechanisms in real materials [45], and our prediction here is more applicable to high-quality samples with low carrier concentrations. We further propose that the orbital magnetization induced by electric field in even SL can result in nonzero MCD signals in the AFM regime. More experimental studies are necessary to validate our prediction of the AH effect in even and odd SL MBT at electron and hole doping, as well as the possibility of electric control of orbital mag-

netization in even SL MBT films.

ACKNOWLEDGEMENT

We would like to acknowledge Binghai Yan for the helpful discussion. R.B. M. and C.-X. L. acknowledges the support through the Penn State MRSEC–Center for Nanoscale Science via NSF award DMR-2011839. Y.-F. Z. and C.-Z. C. acknowledge the support from the ARO Award (W911NF2210159) and the Gordon and Betty Moore Foundation’s EPiQS Initiative (Grant GBMF9063 to C. -Z. C.). D.X. is supported by AFOSR MURI 2D MAGIC (FA9550-19-1-0390).

-
- [1] M. M. Otrokov, T. V. Menshchikova, M. G. Vergniory, I. P. Rusinov, A. Y. Vyazovskaya, Y. M. Koroteev, G. Bihlmayer, A. Ernst, P. M. Echenique, A. Arnau, *et al.*, Highly-ordered wide bandgap materials for quantized anomalous hall and magnetoelectric effects, *2D Materials* **4**, 025082 (2017).
 - [2] J.-Q. Yan, Q. Zhang, T. Heitmann, Z. Huang, K. Y. Chen, J.-G. Cheng, W. Wu, D. Vaknin, B. C. Sales, and R. J. McQueeney, Crystal growth and magnetic structure of MnBi_2Te_4 , *Phys. Rev. Materials* **3**, 064202 (2019).
 - [3] Y. Gong, J. Guo, J. Li, K. Zhu, M. Liao, X. Liu, Q. Zhang, L. Gu, L. Tang, X. Feng, D. Zhang, W. Li, C. Song, L. Wang, P. Yu, X. Chen, Y. Wang, H. Yao, W. Duan, Y. Xu, S.-C. Zhang, X. Ma, Q.-K. Xue, and K. He, Experimental realization of an intrinsic magnetic topological insulator, *Chinese Physics Letters* **36**, 076801 (2019).
 - [4] M. M. Otrokov, I. I. Klimovskikh, H. Bentmann, D. Estyunin, A. Zeugner, Z. S. Aliev, S. Gaß, A. Wolter, A. Koroleva, A. M. Shikin, *et al.*, Prediction and observation of an antiferromagnetic topological insulator, *Nature* **576**, 416 (2019).
 - [5] J. Wu, F. Liu, M. Sasase, K. Ienaga, Y. Obata, R. Yukawa, K. Horiba, H. Kumigashira, S. Okuma, T. Inoshita, *et al.*, Natural van der waals heterostructural single crystals with both magnetic and topological properties, *Science advances* **5**, eaax9989 (2019).
 - [6] M. Shi, B. Lei, C. Zhu, D. Ma, J. Cui, Z. Sun, J. Ying, and X. Chen, Magnetic and transport properties in the magnetic topological insulators $\text{MnBi}_2\text{Te}_4(\text{Bi}_2\text{Te}_3)_n$ ($n=1, 2$), *Physical Review B* **100**, 155144 (2019).
 - [7] K. He, MnBi_2Te_4 -family intrinsic magnetic topological materials, *npj Quantum Materials* **5**, 1 (2020).
 - [8] J. Liu and T. Hesjedal, Magnetic topological insulator heterostructures: A review, *Advanced Materials*, 2102427 (2021).
 - [9] C.-Z. Chang, Marriage of topology and magnetism, *Nature Materials* **19**, 484 (2020).
 - [10] C.-Z. Chang, C.-X. Liu, and A. H. MacDonald, Colloquium: Quantum anomalous hall effect, *Reviews of Modern Physics* **95**, 011002 (2023).
 - [11] M. M. Otrokov, I. P. Rusinov, M. Blanco-Rey, M. Hoffmann, A. Y. Vyazovskaya, S. V. Eremeev, A. Ernst, P. M. Echenique, A. Arnau, and E. V. Chulkov, Unique thickness-dependent properties of the van der waals interlayer antiferromagnet MnBi_2Te_4 films, *Phys. Rev. Lett.* **122**, 107202 (2019).
 - [12] J. Li, Y. Li, S. Du, Z. Wang, B.-L. Gu, S.-C. Zhang, K. He, W. Duan, and Y. Xu, Intrinsic magnetic topological insulators in van der waals layered MnBi_2Te_4 -family materials, *Science Advances* **5**, eaaw5685 (2019).
 - [13] D. Zhang, M. Shi, T. Zhu, D. Xing, H. Zhang, and J. Wang, Topological axion states in the magnetic insulator MnBi_2Te_4 with the quantized magnetoelectric effect, *Phys. Rev. Lett.* **122**, 206401 (2019).
 - [14] R.-X. Zhang, F. Wu, and S. Das Sarma, Möbius insulator and higher-order topology in $\text{MnBi}_{2n}\text{Te}_{3n+1}$, *Phys. Rev. Lett.* **124**, 136407 (2020).
 - [15] Y. J. Chen, L. X. Xu, J. H. Li, Y. W. Li, H. Y. Wang, C. F. Zhang, H. Li, Y. Wu, A. J. Liang, C. Chen, S. W. Jung, C. Cacho, Y. H. Mao, S. Liu, M. X. Wang, Y. F. Guo, Y. Xu, Z. K. Liu, L. X. Yang, and Y. L. Chen, Topological electronic structure and its temperature evolution in antiferromagnetic topological insulator MnBi_2Te_4 , *Phys. Rev. X* **9**, 041040 (2019).
 - [16] D. Estyunin, I. I. Klimovskikh, A. M. Shikin, E. Schwier, M. Otrokov, A. Kimura, S. Kumar, S. Filnov, Z. S. Aliev, M. Babanly, *et al.*, Signatures of temperature driven antiferromagnetic transition in the electronic structure of topological insulator MnBi_2Te_4 , *APL Materials* **8**, 021105 (2020).
 - [17] D. Nevala, H. X. Li, J.-Q. Yan, R. Moore, H.-N. Lee, H. Miao, and P. D. Johnson, Coexistence of surface ferromagnetism and a gapless topological state in MnBi_2Te_4 , *Physical Review Letters* **125**, 117205 (2020).
 - [18] C. Yan, S. Fernandez-Mulligan, R. Mei, S. H. Lee, N. Protic, R. Fukumori, B. Yan, C. Liu, Z. Mao, and S. Yang, Origins of electronic bands in the antiferromagnetic topological insulator MnBi_2Te_4 , *Phys. Rev. B* **104**, L041102 (2021).
 - [19] E. D. Rienks, S. Wimmer, J. Sánchez-Barriga, O. Caha, P. S. Mandal, J. Růžička, A. Ney, H. Steiner, V. V. Volobuev, H. Groiß, *et al.*, Large magnetic gap at the dirac point in $\text{Bi}_2\text{Te}_3/\text{MnBi}_2\text{Te}_4$ heterostructures, *Nature* **576**, 423 (2019).
 - [20] P. Swatek, Y. Wu, L.-L. Wang, K. Lee, B. Schunk, J. Yan, and A. Kaminski, Gapless dirac surface states in the antiferromagnetic topological insulator MnBi_2Te_4 ,

- Phys. Rev. B **101**, 161109 (2020).
- [21] X.-L. Qi and S.-C. Zhang, Topological insulators and superconductors, Reviews of Modern Physics **83**, 1057 (2011).
 - [22] D. Xiao, J. Jiang, J.-H. Shin, W. Wang, F. Wang, Y.-F. Zhao, C. Liu, W. Wu, M. H. Chan, N. Samarth, *et al.*, Realization of the axion insulator state in quantum anomalous hall sandwich heterostructures, Physical review letters **120**, 056801 (2018).
 - [23] Y. Xu, Z. Song, Z. Wang, H. Weng, and X. Dai, Higher-order topology of the axion insulator EuIn_2As_2 , Physical review letters **122**, 256402 (2019).
 - [24] R. Chen, S. Li, H.-P. Sun, Q. Liu, Y. Zhao, H.-Z. Lu, and X. Xie, Using nonlocal surface transport to identify the axion insulator, Physical Review B **103**, L241409 (2021).
 - [25] M. Gu, J. Li, H. Sun, Y. Zhao, C. Liu, J. Liu, H. Lu, and Q. Liu, Spectral signatures of the surface anomalous hall effect in magnetic axion insulators, Nature communications **12**, 1 (2021).
 - [26] C. Liu, Y. Wang, H. Li, Y. Wu, Y. Li, J. Li, K. He, Y. Xu, J. Zhang, and Y. Wang, Robust axion insulator and chern insulator phases in a two-dimensional antiferromagnetic topological insulator, Nature materials **19**, 522 (2020).
 - [27] M. Mogi, M. Kawamura, R. Yoshimi, A. Tsukazaki, Y. Kozuka, N. Shirakawa, K. Takahashi, M. Kawasaki, and Y. Tokura, A magnetic heterostructure of topological insulators as a candidate for an axion insulator, Nature materials **16**, 516 (2017).
 - [28] M. Mogi, M. Kawamura, A. Tsukazaki, R. Yoshimi, K. S. Takahashi, M. Kawasaki, and Y. Tokura, Tailoring tricolor structure of magnetic topological insulator for robust axion insulator, Science advances **3**, eaao1669 (2017).
 - [29] H. Li, H. Jiang, C.-Z. Chen, and X. Xie, Critical behavior and universal signature of an axion insulator state, Physical Review Letters **126**, 156601 (2021).
 - [30] Z.-D. Song, B. Lian, R. Queiroz, R. Ilan, B. A. Bernevig, and A. Stern, Delocalization transition of a disordered axion insulator, Physical review letters **127**, 016602 (2021).
 - [31] K. M. Fijalkowski, N. Liu, M. Hartl, M. Winnerlein, P. Mandal, A. Coschizza, A. Fothergill, S. Grauer, S. Schreyeck, K. Brunner, M. Greiter, R. Thomale, C. Gould, and L. W. Molenkamp, Any axion insulator must be a bulk three-dimensional topological insulator, Phys. Rev. B **103**, 235111 (2021).
 - [32] G. M. Pierantozzi, A. De Vita, C. Bigi, X. Gui, H.-J. Tien, D. Mondal, F. Mazzola, J. Fujii, I. Vobornik, G. Vinai, *et al.*, Evidence of magnetism-induced topological protection in the axion insulator candidate eun_2p_2 , Proceedings of the National Academy of Sciences **119**, e2116575119 (2022).
 - [33] J. Yu, J. Zang, and C.-X. Liu, Magnetic resonance induced pseudoelectric field and giant current response in axion insulators, Physical Review B **100**, 075303 (2019).
 - [34] C. Yue, Y. Xu, Z. Song, H. Weng, Y.-M. Lu, C. Fang, and X. Dai, Symmetry-enforced chiral hinge states and surface quantum anomalous hall effect in the magnetic axion insulator $\text{bi}_2\text{-xsmxse}_3$, Nature Physics **15**, 577 (2019).
 - [35] A. Sekine and K. Nomura, Axion electrodynamics in topological materials, Journal of Applied Physics **129**, 141101 (2021).
 - [36] R. Li, J. Wang, X.-L. Qi, and S.-C. Zhang, Dynamical axion field in topological magnetic insulators, Nature Physics **6**, 284 (2010).
 - [37] B. Chen, F. Fei, D. Zhang, B. Zhang, W. Liu, S. Zhang, P. Wang, B. Wei, Y. Zhang, Z. Zuo, J. Guo, Q. Liu, Z. Wang, X. Wu, J. Zong, X. Xie, W. Chen, Z. Sun, S. Wang, Y. Zhang, M. Zhang, X. Wang, F. Song, H. Zhang, D. Shen, and B. Wang, Intrinsic magnetic topological insulator phases in the sb doped MnBi_2Te_4 bulks and thin flakes, Nature Communications **10**, 4469 (2019).
 - [38] Y. Deng, Y. Yu, M. Z. Shi, Z. Guo, Z. Xu, J. Wang, X. H. Chen, and Y. Zhang, Quantum anomalous hall effect in intrinsic magnetic topological insulator MnBi_2Te_4 , Science **367**, 895 (2020).
 - [39] D. Ovchinnikov, X. Huang, Z. Lin, Z. Fei, J. Cai, T. Song, M. He, Q. Jiang, C. Wang, H. Li, Y. Wang, Y. Wu, D. Xiao, J.-H. Chu, J. Yan, C.-Z. Chang, Y.-T. Cui, and X. Xu, Intertwined topological and magnetic orders in atomically thin chern insulator MnBi_2Te_4 , Nano Letters **21**, 2544 (2021).
 - [40] S. Yang, X. Xu, Y. Zhu, R. Niu, C. Xu, Y. Peng, X. Cheng, X. Jia, Y. Huang, X. Xu, *et al.*, Odd-even layer-number effect and layer-dependent magnetic phase diagrams in MnBi_2Te_4 , Physical Review X **11**, 011003 (2021).
 - [41] J. Cai, D. Ovchinnikov, Z. Fei, M. He, T. Song, Z. Lin, C. Wang, D. Cobden, J.-H. Chu, Y.-T. Cui, *et al.*, Electric control of a canted-antiferromagnetic chern insulator, Nature communications **13**, 1 (2022).
 - [42] J.-X. Qiu, C. Tzschaschel, J. Ahn, A. Gao, H. Li, X.-Y. Zhang, B. Ghosh, C. Hu, Y.-X. Wang, Y.-F. Liu, *et al.*, Axion optical induction of antiferromagnetic order, Nature Materials, 1 (2023).
 - [43] Y.-F. Zhao, L.-J. Zhou, F. Wang, G. Wang, T. Song, D. Ovchinnikov, H. Yi, R. Mei, K. Wang, M. H. W. Chan, C.-X. Liu, X. Xu, and C.-Z. Chang, Even-odd layer-dependent anomalous hall effect in topological magnet MnBi_2Te_4 thin films, Nano Letters **21**, 7691 (2021).
 - [44] A. Gao, Y.-F. Liu, C. Hu, J.-X. Qiu, C. Tzschaschel, B. Ghosh, S.-C. Ho, D. Bérubé, R. Chen, H. Sun, Z. Zhang, X.-Y. Zhang, Y.-X. Wang, N. Wang, Z. Huang, C. Felser, A. Agarwal, T. Ding, H.-J. Tien, A. Akey, J. Gardener, B. Singh, K. Watanabe, T. Taniguchi, K. S. Burch, D. C. Bell, B. B. Zhou, W. Gao, H.-Z. Lu, A. Bansil, H. Lin, T.-R. Chang, L. Fu, Q. Ma, N. Ni, and S.-Y. Xu, Layer hall effect in a 2D topological axion antiferromagnet, Nature **595**, 521 (2021).
 - [45] S. Zhang, R. Wang, X. Wang, B. Wei, B. Chen, H. Wang, G. Shi, F. Wang, B. Jia, Y. Ouyang, F. Xie, F. Fei, M. Zhang, X. Wang, D. Wu, X. Wan, F. Song, H. Zhang, and B. Wang, Experimental observation of the gate-controlled reversal of the anomalous hall effect in the intrinsic magnetic topological insulator MnBi_2Te_4 device, Nano Letters **20**, 709 (2020).
 - [46] D. Huang, C. Chang, H.-T. Jeng, G. Guo, H.-J. Lin, W. Wu, H. Ku, A. Fujimori, Y. Takahashi, and C. Chen, Spin and orbital magnetic moments of Fe_3O_4 , Physical review letters **93**, 077204 (2004).
 - [47] X. Lu, P. Stepanov, W. Yang, M. Xie, M. A. Aamir, I. Das, C. Urgell, K. Watanabe, T. Taniguchi, G. Zhang, *et al.*, Superconductors, orbital magnets and correlated states in magic-angle bilayer graphene, Nature **574**, 653 (2019).
 - [48] A. L. Sharpe, E. J. Fox, A. W. Barnard, J. Finney, K. Watanabe, T. Taniguchi, M. Kastner, and

- D. Goldhaber-Gordon, Emergent ferromagnetism near three-quarters filling in twisted bilayer graphene, *Science* **365**, 605 (2019).
- [49] W.-Y. He, D. Goldhaber-Gordon, and K. T. Law, Giant orbital magnetoelectric effect and current-induced magnetization switching in twisted bilayer graphene, *Nature communications* **11**, 1 (2020).
- [50] Y.-H. Li and R. Cheng, Identifying axion insulator by quantized magnetoelectric effect in antiferromagnetic MnBi_2Te_4 tunnel junction, *Physical Review Research* **4**, L022067 (2022).
- [51] D. Mills and W. Saslow, Surface effects in the heisenberg antiferromagnet, *Physical Review* **171**, 488 (1968).
- [52] Y. Lu, R. Fei, X. Lu, L. Zhu, L. Wang, and L. Yang, Artificial multiferroics and enhanced magnetoelectric effect in van der waals heterostructures, *ACS applied materials & interfaces* **12**, 6243 (2020).
- [53] J. Shang, X. Tang, Y. Gu, A. V. Krasheninnikov, S. Piccozzi, C. Chen, and L. Kou, Robust magnetoelectric effect in the decorated graphene/ In_2Se_3 heterostructure, *ACS Applied Materials & Interfaces* **13**, 3033 (2021).
- [54] D. Xiao, J. Shi, and Q. Niu, Berry phase correction to electron density of states in solids, *Physical review letters* **95**, 137204 (2005).
- [55] I. Souza and D. Vanderbilt, Dichroic f-sum rule and the orbital magnetization of crystals, *Physical Review B* **77**, 054438 (2008).
- [56] D. Xiao, M.-C. Chang, and Q. Niu, Berry phase effects on electronic properties, *Reviews of modern physics* **82**, 1959 (2010).
- [57] T. Thonhauser, Theory of orbital magnetization in solids, *International Journal of Modern Physics B* **25**, 1429 (2011).
- [58] A. M. Essin, J. E. Moore, and D. Vanderbilt, Magneto-electric polarizability and axion electrodynamics in crystalline insulators, *Physical review letters* **102**, 146805 (2009).
- [59] A. M. Essin, A. M. Turner, J. E. Moore, and D. Vanderbilt, Orbital magnetoelectric coupling in band insulators, *Physical Review B* **81**, 205104 (2010).
- [60] J. Wang, B. Lian, X.-L. Qi, and S.-C. Zhang, Quantized topological magnetoelectric effect of the zero-plateau quantum anomalous hall state, *Physical Review B* **92**, 081107 (2015).
- [61] F. Wilczek, Two applications of axion electrodynamics, *Physical Review Letters* **58**, 1799 (1987).
- [62] X.-L. Qi, T. L. Hughes, and S.-C. Zhang, Topological field theory of time-reversal invariant insulators, *Physical Review B* **78**, 195424 (2008).
- [63] R.-X. Zhang, F. Wu, and S. D. Sarma, Möbius insulator and higher-order topology in $\text{MnBi}_{2n}\text{Te}_{3n+1}$, *Physical review letters* **124**, 136407 (2020).
- [64] B. J. Wieder and B. A. Bernevig, The axion insulator as a pump of fragile topology, *arXiv preprint arXiv:1810.02373* (2018).
- [65] N. Varnava and D. Vanderbilt, Surfaces of axion insulators, *Physical Review B* **98**, 245117 (2018).
- [66] N. Varnava, J. H. Wilson, J. Pixley, and D. Vanderbilt, Controllable quantum point junction on the surface of an antiferromagnetic topological insulator, *Nature communications* **12**, 1 (2021).
- [67] J. Ahn, S.-Y. Xu, and A. Vishwanath, Theory of optical axion electrodynamics and application to the kerr effect in topological antiferromagnets, *Nature Communications* **13**, 1 (2022).
- [68] P. M. Sass, W. Ge, J. Yan, D. Obeysekera, J. Yang, and W. Wu, Magnetic imaging of domain walls in the antiferromagnetic topological insulator mnbi_2te_4 , *Nano Letters* **20**, 2609 (2020).
- [69] E. Novik, A. Pfeuffer-Jeschke, T. Jungwirth, V. Latussek, C. Becker, G. Landwehr, H. Buhmann, and L. Molenkamp, Band structure of semimagnetic $\text{Hg}_{1-y}\text{Mn}_y\text{Te}$ quantum wells, *Physical Review B* **72**, 035321 (2005).
- [70] C.-X. Liu, X.-L. Qi, H. Zhang, X. Dai, Z. Fang, and S.-C. Zhang, Model hamiltonian for topological insulators, *Physical Review B* **82**, 045122 (2010).
- [71] D. Xiao, W. Yao, and Q. Niu, Valley-contrasting physics in graphene: magnetic moment and topological transport, *Physical review letters* **99**, 236809 (2007).

Supplemental Materials

I. MODEL HAMILTONIANS FOR MBT FILMS

MnBi₂Te₄ (MBT) is a layered topological insulator with anti-ferromagnetic (AFM) coupling between adjacent septuple layers (SLs). Here we use two models to simulate such MBT films. In a two-surface-state model, we only consider the top and bottom surfaces of the film described by two Dirac Hamiltonians. We further introduce exchange couplings, magnetization, gauge couplings and external magnetic fields, as well as an asymmetric potential induced by external electric fields (gate voltages). The AFM order implies that the magnetizations on the two surfaces are parallel for odd SL MBT films and anti-parallel for even SL films (Fig. S1(a)). In a thin-film model, we employ an effective four-band model for a bulk magnetic topological insulator and construct a slab model for the thin film along z direction with the open boundary condition for the four-band model Hamiltonian (Fig. S2(a)). The exchange coupling is a z -dependent function that implements the AFM order between neighboring layers. We further investigate the Landau levels and anomalous Hall (AH) effect for both models in the following sections.

A. Two surface state models

As described in the main text, the two-surface-state model in the basis $|t, \uparrow\rangle$, $|t, \downarrow\rangle$, $|b, \uparrow\rangle$ and $|b, \downarrow\rangle$ writes as

$$H = v_f((k_x + \frac{e}{\hbar}A_x)\sigma_y - (k_y + \frac{e}{\hbar}A_y)\sigma_x)\tau_z + V_0\tau_z/2 + gM_s \begin{pmatrix} m_{1,z}\sigma_z & 0 \\ 0 & m_{2,z}\sigma_z \end{pmatrix}, \quad (\text{S1})$$

where τ and σ are Pauli matrices in the layer and spin sub-space, respectively, $m_{i,z} = \pm 1$ are the magnetization vectors of the top ($i = 1$) and bottom ($i = 2$) surfaces (in even SL, $m_{1,z} = -1$ corresponds to AFM1, $m_{1,z} = +1$ corresponds to AFM2 and $m_{2,z} = -m_{1,z}$), and g is the exchange coupling coefficient. Below we will solve the Landau level spectrum of this model Hamiltonian.

Under the presence of an out-of-plane magnetic field $\mathbf{B} = (0, 0, B)$, Landau levels (LLs) emerge from the bands [69]. We choose the Landau gauge as $\mathbf{A} = (0, Bx, 0)$ with $B > 0$ and substitute k_x and k_y with the annihilation and creation operators

$$a = \frac{l_c}{\sqrt{2}}k_-, a^\dagger = \frac{l_c}{\sqrt{2}}k_+, \quad (\text{S2})$$

where $k_\pm = k_x \pm ik_y$ and $l_c = \sqrt{\frac{\hbar}{eB}}$ is the magnetic length. On the harmonic oscillator basis ϕ_n with $n = 0, 1, 2, \dots$, these operators behave as

$$a\phi_n = \sqrt{n}\phi_{n-1}, a^\dagger\phi_n = \sqrt{n+1}\phi_{n+1}, a^\dagger a\phi_n = n\phi_n. \quad (\text{S3})$$

By replacing k_x and k_y with a and a^\dagger in Eq. (S1), we then obtain the Hamiltonian and the wave-function ansatz[69],

$$H = \begin{pmatrix} V_0/2 + gM_s m_{1,z} & -i\sqrt{2}v_f a/l_c & 0 & 0 \\ i\sqrt{2}v_f a^\dagger/l_c & V_0/2 - gM_s m_{1,z} & 0 & 0 \\ 0 & 0 & -V_0/2 + gM_s m_{2,z} & i\sqrt{2}v_f a/l_c \\ 0 & 0 & -i\sqrt{2}v_f a^\dagger/l_c & -V_0/2 - gM_s m_{2,z} \end{pmatrix}, \quad (\text{S4})$$

$$\Psi_N = \exp(-iXy/l_c^2) \begin{pmatrix} f_1^N \phi_N \\ f_2^N \phi_{N+1} \\ f_3^N \phi_N \\ f_4^N \phi_{N+1} \end{pmatrix}, \quad (\text{S5})$$

where $N = -1, 0, 1, \dots$ as n ranges from $0, 1, 2, \dots$, $X = -k_y l_c^2$ is the center of motion and f_i^N are the expansion

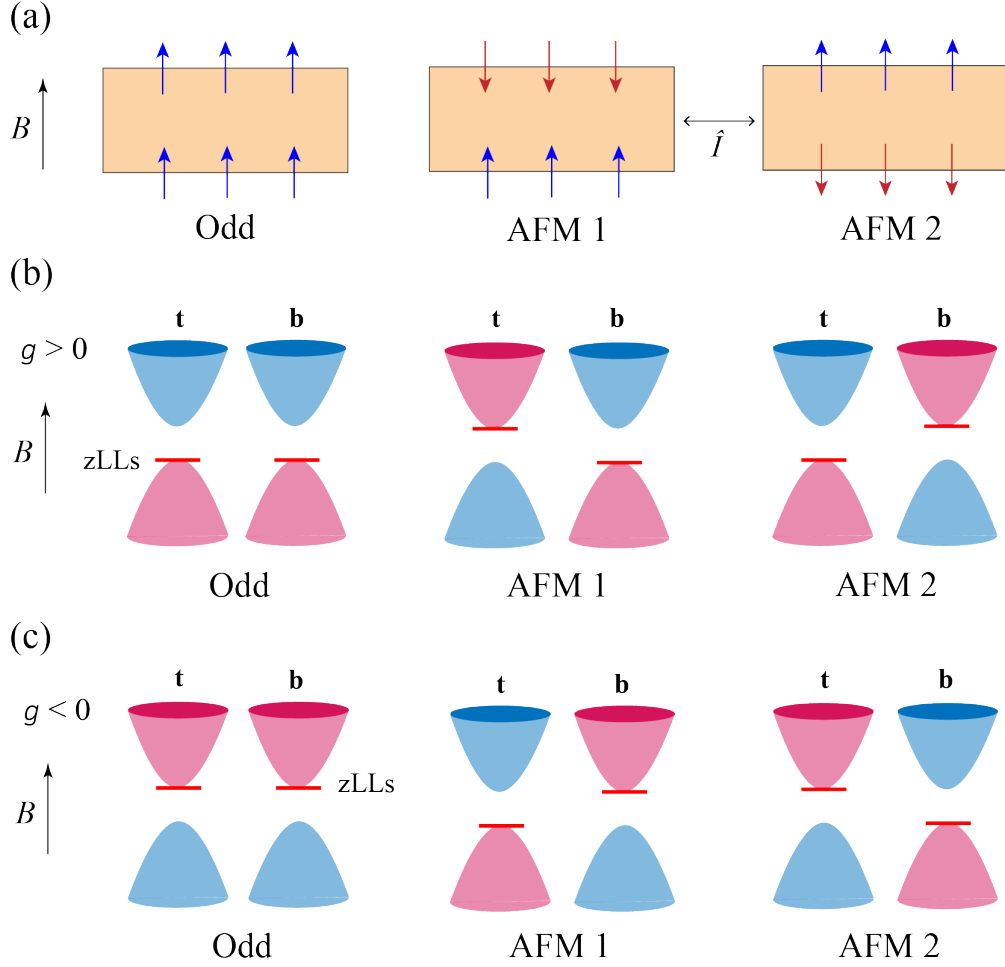


FIG. S1. (a) Illustration of the magnetization configurations for odd and even SL AFM MBT films. In odd SL, the magnetization of both surfaces aligns with the external magnetic field. In even SL, there are two possible AFM configurations with opposite magnetization on top and bottom surfaces. (b) The positions of zLLs in two-surface-state model for $g > 0$ and $B > 0$. The bands are labeled with red and blue colors which represent negative and positive AH signs, respectively. (c) The locations of zLLs for $g < 0$ and $B < 0$.

coefficients in the harmonic oscillator basis. From the Hamiltonian with $N = -1$

$$H^{N=-1} = \begin{pmatrix} 0 & 0 & 0 & 0 \\ 0 & V_0/2 - gM_s m_{1,z} & 0 & 0 \\ 0 & 0 & 0 & 0 \\ 0 & 0 & 0 & -V_0/2 - gM_s m_{2,z} \end{pmatrix}, \quad (S6)$$

$$\Psi_{N=-1} = \begin{pmatrix} 0 \\ \phi_0 \\ 0 \\ \phi_0 \end{pmatrix},$$

we can solve the zeroth Landau levels (zLLs) as $\varepsilon_t = V_0/2 - gM_s m_{1,z}$ and $\varepsilon_b = -V_0/2 - gM_s m_{2,z}$ for the top and

bottom surface state, respectively. The higher Landau levels are obtained from the Hamiltonian

$$H^N = \begin{pmatrix} V_0/2 + gM_s m_{1,z} & \frac{-iv_f \sqrt{2(N+1)}}{l_c} & 0 & 0 \\ \frac{iv_f \sqrt{2(N+1)}}{l_c} & V_0/2 - gM_s m_{1,z} & 0 & 0 \\ 0 & 0 & -V_0/2 + gM_s m_{2,z} & \frac{iv_f \sqrt{2(N+1)}}{l_c} \\ 0 & 0 & \frac{-iv_f \sqrt{2(N+1)}}{l_c} & -V_0/2 - gM_s m_{2,z} \end{pmatrix}. \quad (S7)$$

B. Thin film model

We then considered a MBT thin film based on an effective bulk four-band model [70]. The intrinsic AFM orders are implemented such that the neighboring layers have opposite exchange coupling g . To simplify the case, here we introduce the 2 SL film, with a total thickness L and septuple-layer (SL) thickness d (Fig. S2(a)). The samples with any layers can be calculated with the same method.

The effective four-band Hamiltonian for 2 SL film writes as

$$\begin{aligned} H &= H_0 + H_1 + H_2, \\ H_0 &= M(\mathbf{k})\tau_z + Bk_z\tau_y + A((k_y + \frac{e}{\hbar}A_y)\tau_x\sigma_x - (k_x + \frac{e}{\hbar}A_x)\tau_x\sigma_y), \\ H_1 &= -e(Ez - Ed)\sigma_0 = (V_0z/L - V_0/2)\sigma_0, \\ H_2 &= \begin{cases} gM_s m_{s1,z}\sigma_z, & L/2 < z < L, \\ gM_s m_{s2,z}\sigma_z, & 0 < z < L/2 \end{cases}, \end{aligned} \quad (S8)$$

where the four-band model H_0 is written in the basis $|P1^+, \uparrow\rangle$, $|P2^+, \uparrow\rangle$, $|P1^+, \downarrow\rangle$ and $|P2^+, \downarrow\rangle$ with Pauli matrices τ and σ in the orbital ($P1, P2$) and spin (\uparrow, \downarrow) sub-space, $M(\mathbf{k}) = M_0 + M_1k_z^2 + M_2k_{\parallel}^2$, E is the electric field strength and V_0 is the asymmetric potential drop across the whole thin film. For the thin film model, the z -directional momentum k_z should be replaced by $-i\partial_z$ with open boundary condition $\psi_{k_{\parallel}}(z=0) = \psi_{k_{\parallel}}(z=L) = 0$, and the wavefunction is then expanded as

$$\psi_{k_{\parallel}}(z) = \sum_{n,\lambda} a_{n,\lambda}(k_{\parallel}) \sqrt{\frac{2}{L}} \sin(\frac{n\pi}{L}z) |\lambda\rangle, \quad (S9)$$

where $n = 1, 2, \dots, N$, $a_{n,\lambda}(k_{\parallel})$ is the expansion coefficient and $|\lambda\rangle$ is the basis of the four-band model with $\lambda = 1, \dots, 4$. Combined with the eigen-equation $H(k_{\parallel})\psi_{k_{\parallel}}(z) = E\psi_{k_{\parallel}}(z)$, we obtain the matrix element of expansion

$$\langle n, \lambda | H | n', \lambda' \rangle = \frac{2}{L} \int_0^L dz \sin(\frac{n\pi}{L}z) H_{\lambda\lambda'}(z) \sin(\frac{n'\pi}{L}z). \quad (S10)$$

We chose the parameters as $M_0 = -0.28\text{eV}$, $M_1 = 6.86\text{eV}\text{\AA}^2$, $M_2 = 44.5\text{eV}\text{\AA}^2$, $A = 3.33\text{eV}\text{\AA}$, $B = 2.26\text{eV}\text{\AA}$, $N = 15$ and $d = 1.3\text{nm}$ [70].

We examined the effect of E and B on determining the favored AFM configuration by calculating Landau levels following the same method as shown in the last section. The difference is that now the Hamiltonian has z dependence, and thus the eigen-wave function ansatz should take the form [69]

$$\Psi_N = \exp(-iXy/l_c^2) \begin{pmatrix} f_1^N(z)\phi_N \\ f_2^N(z)\phi_N \\ f_3^N(z)\phi_{N+1} \\ f_4^N(z)\phi_{N+1} \end{pmatrix}, \quad (S11)$$

where all the f_i^N are z -dependent functions. By solving the Hamiltonian, we plot the dispersion and the energy of LLs as a function of B at $gM_s = 0.05\text{eV}$ ($g > 0$) and $V_0 = 0.1\text{eV}$, as shown in Fig. S2(b) and (c). We summarized the energy difference $\Delta\varepsilon = \varepsilon_{AFM1} - \varepsilon_{AFM2}$ between two configurations as functions of both B and V_0 in Fig. 2(b) in the main text.

In Fig. S2(d), we show the dispersion and Landau levels for 3-SL MBT film with $gM_s = 0.05\text{eV}$ ($g > 0$) and $V_0 = 0.1\text{eV}$. As the zero-field AH resistance and the ordinary Hall resistance share the same sign for the electron

doping in 3-SL MBT film in experiments, this fact is consistent with our Landau level spectrum in Fig. S2(d), in which the zeroth Landau level coincides with the top of the valence bands at small magnetic fields. In our calculation for Fig. S2(d), we choose $g > 0$, while the zeroth Landau level will appear at the conduction band bottom if $g < 0$. Therefore, by comparing the numerical results with the experiment facts, we can fix the sign of the exchange coupling constant as positive within the definition of our model Hamiltonian, and this allows us to determine the anomalous Hall sign in the next section.

The Hall conductance shown in the main text Fig. 2 is calculated by

$$\sigma_{xy} = -i \frac{1}{2\pi} \sum_{\text{filled } n} \int dk_x dk_y \sum_m \frac{\langle u_n | \partial_x H | u_m \rangle \langle u_m | \partial_y H | u_n \rangle - \langle u_n | \partial_y H | u_m \rangle \langle u_m | \partial_x H | u_n \rangle}{(\varepsilon_n - \varepsilon_m)^2}, \quad (\text{S12})$$

where $\partial_j = \frac{\partial}{\partial k_j}$ ($j = x, y$), ε_n and u_n are eigenvalues and eigenvectors of the Hamiltonian and n, m are band numbers.

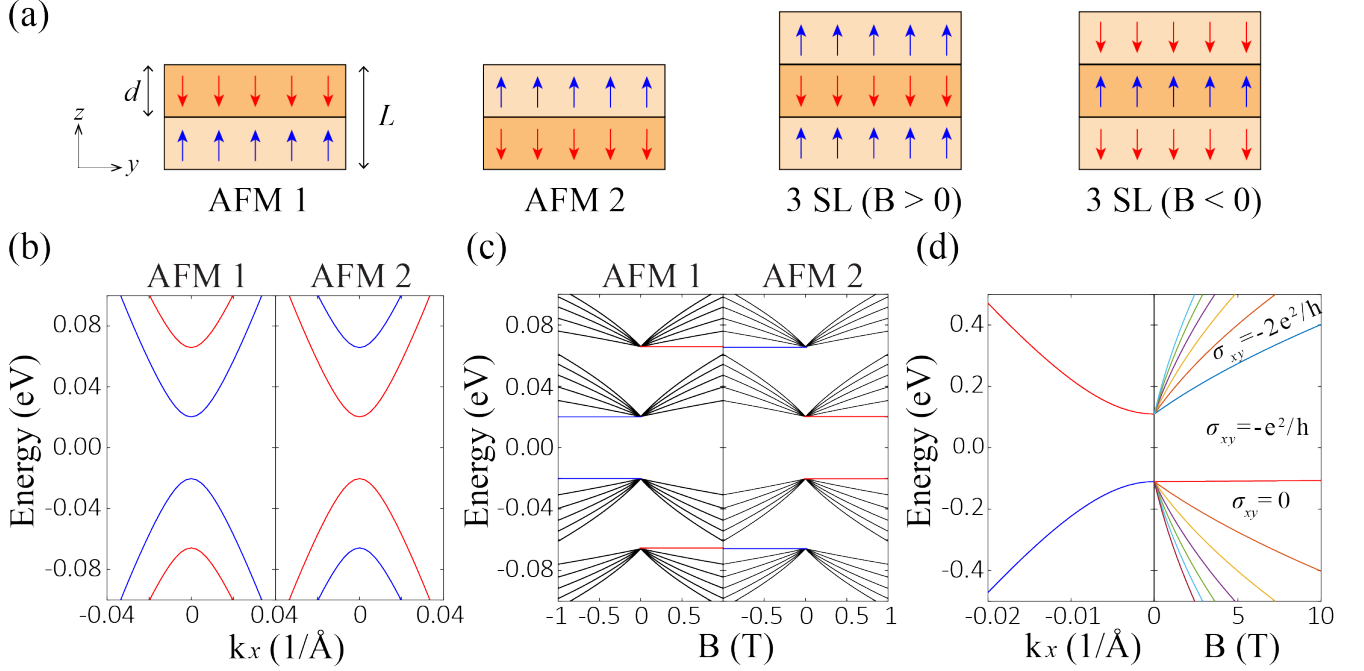


FIG. S2. (a) Illustrations of the thin film model for 2 SL and 3 SL MBT films. The samples have a total thickness of L with each septuple layer thickness $d = 1.3\text{nm}$. The neighboring layers exhibit opposite magnetization to describe AFM order. (b) Electronic energy dispersion for the AFM1 and AFM2 configurations with $gM_s = 0.05\text{eV}$ and $V_0 = 0.1\text{eV}$. (c) The energy spectrum of Landau levels as a function of magnetic field B for the AFM1 and AFM2 configurations. The zeroth Landau levels are labeled in red and blue, while all the higher Landau levels are labeled in black. (d) Dispersion and Landau levels for 3 SL at $gM_s = 0.05\text{eV}$ and $V_0 = 0.1\text{eV}$. The Hall conductance is $\sigma_{xy} = -\frac{e^2}{h}$ in the gap. Note that here we fix chemical potential instead of electron density when considering the Hall resistance at different magnetic fields.

II. ANOMALOUS HALL SIGN

Below we will provide a discussion on the anomalous Hall sign of two AFM configurations in the two-surface-state model. From the Landau level calculations in Sec. I A for the two-surface-state model, we notice that the zeroth LLs only appear for half of the bands and their locations depend on the sign of g and $m_{i,z}$, with $\varepsilon_t = V_0/2 - gM_s m_{1,z}$ and $\varepsilon_b = -V_0/2 - gM_s m_{2,z}$ for the top and bottom surface state. We first focus on the $g > 0$ case. For $B > 0$ and $V_0 = 0$, the magnetization vectors $m_{i,z}$ in odd SL (FM alignment of magnetization between two surfaces) tend to align with the magnetic field, meaning that $m_{1,z} = m_{2,z} = +1$, and thus the zLLs coincide with the energy of valence band top on both top and bottom surfaces with $\varepsilon_t = -gM_s$ and $\varepsilon_b = -gM_s$. In AFM1 with $m_{1,z} = -1$ and $m_{2,z} = +1$, the zLLs are located at the conduction band bottom on the top surface $\varepsilon_t = gM_s$, and valence band top on the bottom surface $\varepsilon_b = -gM_s$. In AFM2, the zLLs are located at the valence band top on the top surface $\varepsilon_t = -gM_s$ and

conduction band bottom on the bottom surface $\varepsilon_b = gM_s$. Meanwhile, we label the AH sign in terms of color red and blue for negative and positive AH signs, respectively, as shown in Fig. S1(b). In odd SL MBT films, the valence bands are assigned with negative AH sign (red) and the conduction bands are assigned with positive AH sign (blue), and thus the zero-field AH resistance should be negative, which is the same as the ordinary Hall resistance (negative for $B > 0$), to be consistent with the AH sign determined from Fig. S2(d), as compared with experiments. As the top surface state of AFM1 and the bottom surface state of AFM2 have opposite magnetization compared to the odd SL, the AH signs of their bands switch correspondingly, namely, the valence band is positive (blue) and the conduction band is negative (red), as shown in Fig. S1(b). Furthermore, the position of the zLL of these surface states also change from valence to conduction band as $m_{i,z}$ changes sign, and therefore, all the zLLs are located at the red bands for $g > 0$ and $B > 0$ (Fig. S1(b)).

Next we will determine the favored AFM configuration for even SL and its AH sign under the presence of an asymmetric potential. The external electric field splits the energies of the top and bottom surface states, and subsequently differentiates the energies of the occupied zLL in AFM1 and AFM2. If electric field lowers the energy of the bottom surface states but increases the energy of the top surface states ($E < 0$ and $V_0 > 0$), then the energy of the occupied zLL for AFM1 $\varepsilon_b = -V_0/2 - gM_s$ decreases, while the energy of the occupied zLL for AFM2 $\varepsilon_t = V_0/2 - gM_s$ increases. Thus, AFM1 becomes energetically favored for $g > 0$, $B > 0$ and $E < 0$ (Fig. S3(b)). More generally, the energetically favored AFM configuration should have its zLL located at the valence band top of the surface state whose energy is lowered by the electric field. Since all the zLLs coincide with the red bands, this means that the favored AFM configuration is the one with red valence band on the lower-energy surface state, as shown in Fig. S3(a) and (b). For electron doping in the favored AFM configuration, the electrons will first fill the conduction band of the lower-energy surface states which should have blue color, as the corresponding valence band has red color. As a result, the overall AH sign is positive (blue) in the favored even SL configuration, opposite to the AH sign in odd SL, which is always negative for $g > 0$ and $B > 0$. Therefore, the even and odd SL have opposite AH signs for the electron doping, irrespective of the electric field direction. For the hole doping, the blue valence band (positive AH sign) of the higher-energy surface state contribute less to AH conductance, so the overall AH sign will be negative, which is the same as the AH sign of odd SL. Based on the above analysis, we sketch the hysteresis loops for odd and even SL at electron and hole dopings in Fig. S4, and we notice that only the even SL at electron doping shows different zero-field AH sign compared to the other cases. For odd SL at electron doping, the ordinary Hall and the AH resistance share the same sign (Fig. S4(a)); while at hole doping, the ordinary Hall resistance has opposite sign as the AH resistance (Fig. S4(b)) and as a result there is a sign change when the magnetic field reduces from a large positive value toward zero. For even SL at electron doping, the AH of FM state and the ordinary Hall have the same sign, and the sign changes happen at a transition from FM state to AFM state and another transition between two AFM states (Fig. S4(c)), which has been discussed in details in the main text. At hole doping, the FM state and AFM state of even SL share the same AH sign, while the ordinary Hall switches sign, and therefore when the magnetic field is reduced from a large positive value toward negative, the Hall resistance changes sign first from ordinary Hall to FM state, followed by another sign change caused by transition between two AFM states (Fig. S4(d)).

On the other hand, for the $g < 0$ case, the location of zLLs in odd SL changes to the conduction band bottom on both surfaces when g changes sign (for $B > 0$ in Fig. S1(c)). Meanwhile, the AH signs of the bands change as well, since the AH signs depend on the sign of $gm_{i,z}$. Therefore, in odd SL, the valence bands have positive AH sign and the conduction bands have negative sign, and thus the zero-field AH resistance should be positive when the Fermi energy is around the gap for $g < 0$. We notice this AH sign in this case is opposite to the ordinary Hall sign at the electron doping, so it is inconsistent with the experimental observations. But we will still discuss the possible scenario for the even SL case when $g < 0$.

For AFM1 of the even SL case, the zLLs are located at the valence band top on the top surface $\varepsilon_t = gM_s$ (M_s is always assumed to be positive), and the conduction band bottom on the bottom surface $\varepsilon_b = -gM_s$. For AFM2 of the even SL case, they are located at the conduction band bottom on the top surface $\varepsilon_t = -gM_s$ and valence band top on the bottom surface $\varepsilon_b = gM_s$. Thus, no matter the sign of g , the locations of the zLLs always coincide with the band energy extreme of the red bands in Fig. S3. Similar to the discussion above for the $g > 0$ case, we find the energetically favored state for the $g < 0$ case is AFM1 when B and E are parallel, and AFM2 when B and E are anti-parallel, in Fig. S3(c) and (d). At electron doping, we notice that the Fermi energy will always cross the blue conduction band of the energetically favored magnetic configuration, no matter this configuration is AFM1 (Fig. S3(c)) or AFM2 (Fig. S3(d)). Consequently, the AH sign is always positive at electron doping, determined by the blue conduction bands, in both Fig. S3(c) and (d). Therefore, for $g < 0$, the even and odd SL show the same positive AH sign at electron doping; while at hole doping, the odd SL still has positive AH sign but the even SL has negative AH sign.

The sign of the exchange coupling g can be determined from comparing the signs of the ordinary Hall and AH resistance in odd SL to those in experiments, as discussed in Sec. IB. For $g > 0$, the ordinary Hall and AH share the same sign, which is consistent with experimental measurements, while for $g < 0$, they have opposite signs for odd

SLs. Therefore, we can fix the sign of exchange coupling as positive (within our definition of the model). Our above analysis further suggests that the odd and even SL films show opposite AH signs at electron doping and the same sign at hole doping for $g > 0$, which is also consistent with experimental observations.

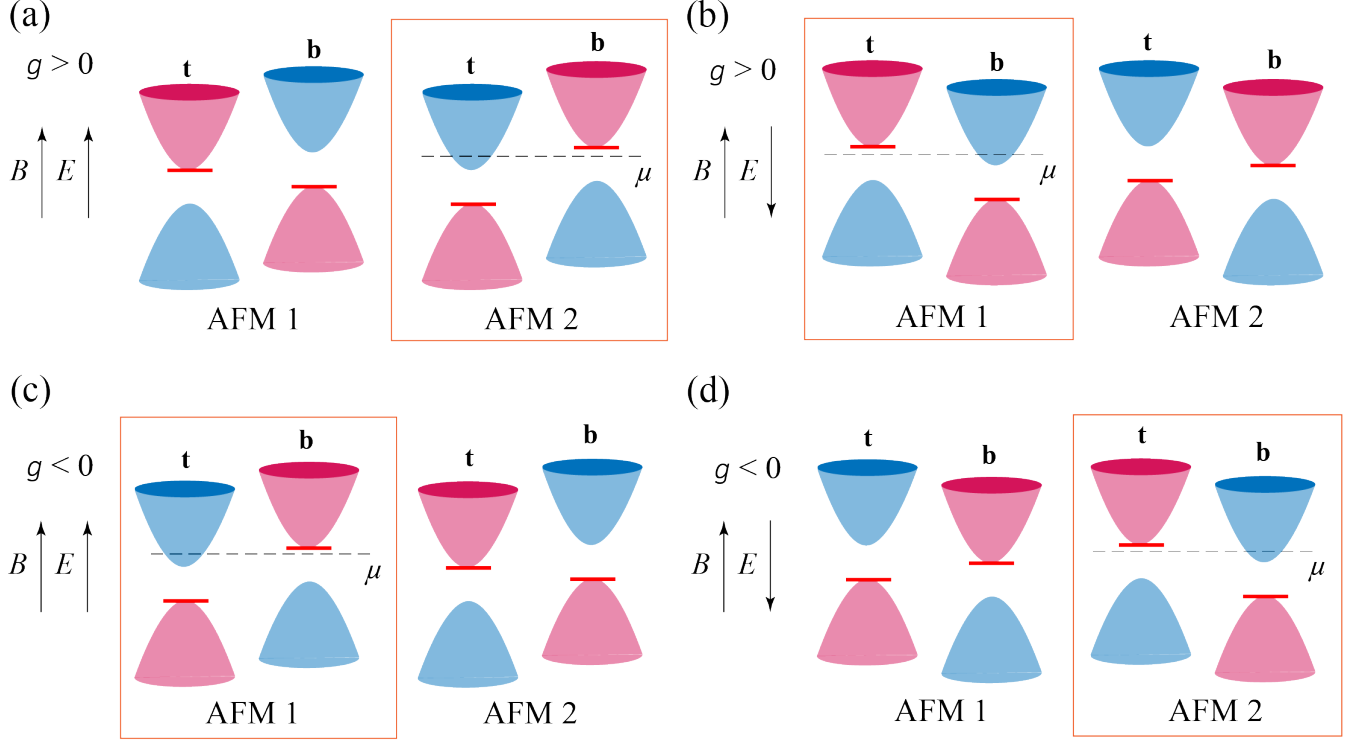


FIG. S3. Illustration of two-surface-state model for AFM1 and AFM2 at (a) $g > 0$ and $B > 0$ and $E > 0$, (b) $g > 0$, $B > 0$ and $E < 0$, (c) $g < 0$ and $B > 0$ and $E > 0$, (d) $g < 0$, $B > 0$ and $E < 0$. The favored AFM configuration in each case is marked by the box.

III. ORBITAL MAGNETIZATION IN MBT FILMS

In this section, we look into the orbital magnetization and axion dynamics in MBT films. As mentioned in the main text, the orbital magnetization contains two parts $m_{total} = m_{tri} + m_{topo}$, a trivial part and a topological part,

$$\begin{aligned}
 m_{tri} &= -\frac{ie}{2\hbar} \langle \nabla_k u | \times [H(k) - \epsilon(k)] | \nabla_k u \rangle \\
 &= -\frac{ie}{2\hbar} \sum_{u'} \frac{\langle u | \partial_x H | u' \rangle \langle u' | \partial_y H | u \rangle - \langle u | \partial_y H | u' \rangle \langle u' | \partial_x H | u \rangle}{\epsilon' - \epsilon},
 \end{aligned} \tag{S13}$$

$$\begin{aligned}
 m_{topo} &= -\frac{ie}{2\hbar} \langle \nabla_k u | \times 2[\epsilon(k) - \mu] | \nabla_k u \rangle \\
 &= -\frac{ie}{\hbar} [\epsilon(k) - \mu] \sum_{u'} \frac{\langle u | \partial_x H | u' \rangle \langle u' | \partial_y H | u \rangle - \langle u | \partial_y H | u' \rangle \langle u' | \partial_x H | u \rangle}{(\epsilon' - \epsilon)^2},
 \end{aligned} \tag{S14}$$

where ϵ and $|u\rangle$ are the eigenvalues and eigenstates of the Hamiltonian in Eq. (S1). For the two-surface-state model, we can derive the orbital magnetic moments analytically following Ref. [71]. Let us consider only the top surface state $H_t = v_f(k_x \sigma_y - k_y \sigma_x) + gM_s m_{1,z} \sigma_z + V_0/2$. The two eigenvalues are $\epsilon_1 = V_0/2 - A$ and $\epsilon_2 = V_0/2 + A$ with

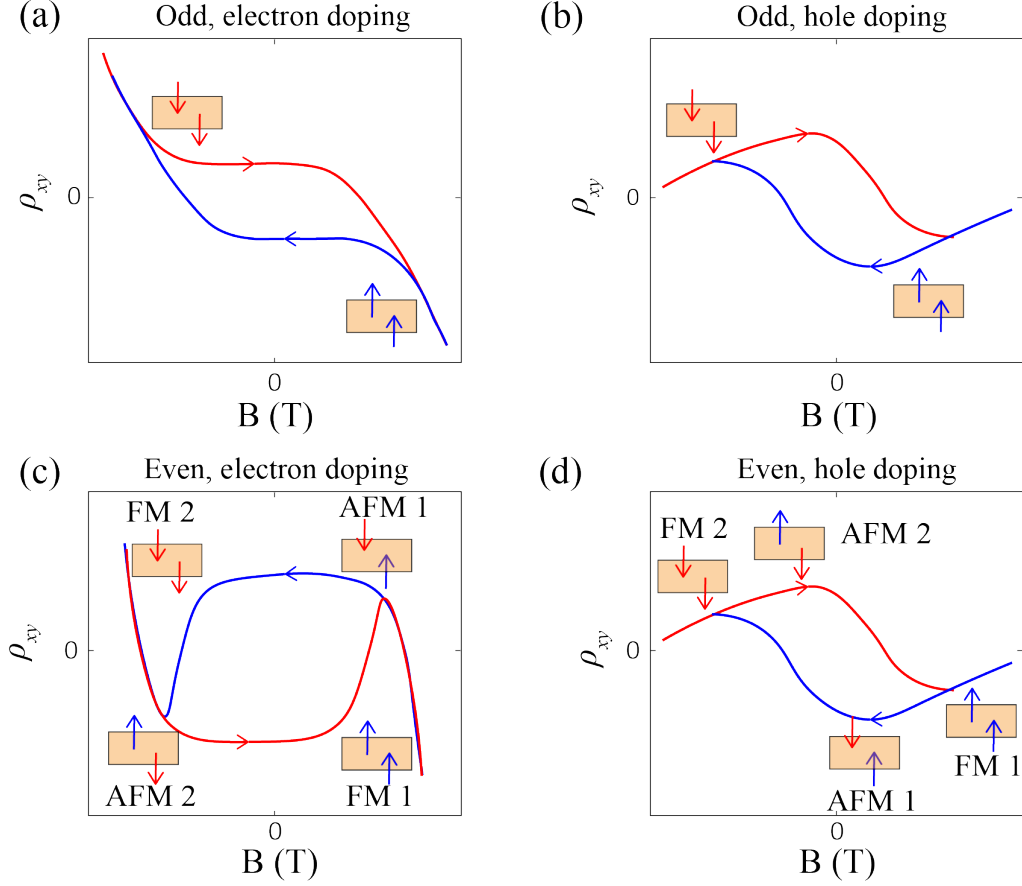


FIG. S4. Predictions of AH hysteresis loops for odd and even SL MBT films at electron and hole doping for $g > 0$. (a) Odd SL at electron doping. The AH sign changes from negative to positive when B sweeps from positive to negative. (b) Even SL at electron doping. The favored AFM configuration has a positive AH sign, so it changes from negative to positive as the system transits from the FM state into AFM state when B decreases from a positive value. Notably, there exists a sign change originating from the transition between two AFM states before the spin-flop transition. (c) Odd SL at hole doping, at which the ordinary Hall has positive slopes. (d) Even SL at hole doping. It shows a similar pattern as the odd SL since they have the same AH sign.

$A = \sqrt{(gM_s)^2 + v_f^2 k^2}$ and the corresponding eigenstates are

$$\begin{aligned} u_1 &= \frac{1}{\sqrt{v_f^2 k^2 + (gM_s m_{1,z} - A)^2}} \begin{pmatrix} gM_s m_{1,z} - A \\ ik_+ v_f \end{pmatrix}, \\ u_2 &= \frac{1}{\sqrt{v_f^2 k^2 + (gM_s m_{1,z} + A)^2}} \begin{pmatrix} gM_s m_{1,z} + A \\ ik_+ v_f \end{pmatrix}, \end{aligned} \quad (\text{S15})$$

with $k_{\pm} = k_x \pm ik_y$. We can then derive

$$\langle u_1 | \partial_x H | u_2 \rangle \langle u_2 | \partial_y H | u_1 \rangle - \langle u_1 | \partial_y H | u_2 \rangle \langle u_2 | \partial_x H | u_1 \rangle = -i \frac{8}{N^2} v_f^4 k_+ k_- gM_s m_{1,z} A, \quad (\text{S16})$$

where $N = \sqrt{(v_f^2 k^2 + (gM_s m_{1,z} - A)^2)(v_f^2 k^2 + (gM_s m_{1,z} + A)^2)} = \sqrt{4v_f^2 k^2 (v_f^2 k^2 + (gM_s)^2)}$. Using Eq. (S13) and (S14), we obtain the orbital magnetic moments of the valence band

$$m_{tri, top} = -\frac{ev_f^2 gM_s m_{1,z}}{2\hbar((gM_s)^2 + v_f^2 k^2)}, \quad (\text{S17})$$

$$m_{topo,top} = \frac{ev_f^2 g M_s m_{1,z}}{2\hbar((gM_s)^2 + v_f^2 k^2)^{3/2}} (\sqrt{(gM_s)^2 + v_f^2 k^2} + \mu - V_0/2) \quad (S18)$$

for the top surface states. Similarly, we can get the analytical results for the bottom surface state $H_b = -v_f(k_x\sigma_y - k_y\sigma_x) + gM_sm_{2,z}\sigma_z - V_0/2$ as

$$m_{tri,bot} = -\frac{ev_f^2 g M_s m_{2,z}}{2\hbar((gM_s)^2 + v_f^2 k^2)}, \quad (S19)$$

$$m_{topo,bot} = \frac{ev_f^2 g M_s m_{2,z}}{2\hbar((gM_s)^2 + v_f^2 k^2)^{3/2}} (\sqrt{(gM_s)^2 + v_f^2 k^2} + \mu + V_0/2). \quad (S20)$$

Therefore, the sum of contributions from the top and bottom surface states is

$$m_{tri} = -\frac{ev_f^2 g M_s}{2\hbar((gM_s)^2 + v_f^2 k^2)} (m_{1,z} + m_{2,z}), \quad (S21)$$

$$m_{topo} = \frac{ev_f^2 g M_s}{2\hbar((gM_s)^2 + v_f^2 k^2)^{3/2}} [(m_{1,z} + m_{2,z})(\sqrt{(gM_s)^2 + v_f^2 k^2} + \mu) + (m_{2,z} - m_{1,z})V_0/2]. \quad (S22)$$

As a result, for odd SL ($m_{1,z} = m_{2,z} = +1$) at $\mu = 0$, there is $m_{tri} = -\frac{ev_f^2 g M_s}{\hbar((gM_s)^2 + v_f^2 k^2)}$ and $m_{topo} = \frac{ev_f^2 g M_s}{\hbar((gM_s)^2 + v_f^2 k^2)}$ which cancel out exactly with each other and lead to zero total orbital magnetization. This is consistent with the result in Ref. [71]. For even SL ($m_{1,z} = -m_{2,z}$), we can see that the trivial part is zero while the topological part is $m_{topo} = \frac{ev_f^2 g M_s m_{2,z} V_0}{2\hbar((gM_s)^2 + v_f^2 k^2)^{3/2}}$, with $m_{2,z} = 1$ for AFM1 and $m_{2,z} = -1$ for AFM2. We emphasize that these results are only valid when there is no coupling between two surface states, while in the numerical calculations of the thin-film model in the main text, a small trivial part of orbital magnetic moment can still be induced due to the hybridization between two surface states, as discussed below.

The hybridization between two surface states can be taken into account by the Hamiltonian $H_t = t\tau_x$ in addition to the Hamiltonian (1) and numerically calculate orbital magnetic moment density in the two-surface-state model. Fig. S5 and Fig. S6 plot the two parts of the orbital magnetic moment and their sum as a function of V_0 at $\mu = 0\text{eV}$ and $\mu = 0.1\text{eV}$, respectively. Here we show the results of AFM1 configuration for even SL, and the orbital magnetization of AFM2 simply flips in sign compared to AFM1. In Fig. S5 ($\mu = 0\text{eV}$), when two surfaces are isolated ($t = 0\text{eV}$), for even SL, the trivial part vanishes and the topological part increases linearly with electric potential V_0 , and the slope represents a quantized magnetoelectric coefficient $\alpha = e^2/2h$. On the other hand, in odd SL both components of orbital magnetic moment are constant and the total magnetic moment is zero, consistent with the analytical results as shown previously. When there is coupling between two surfaces (Fig. S5(b) and (d)), α remains zero for odd SL, while in even SL, the trivial orbital magnetization now presents a nonzero slope with an opposite sign compared to the topological part and thus the total α value is smaller than the quantized value $e^2/2h$, indicating the finite size effect in thin samples where the two surfaces are hybridized. In Fig. S6 ($\mu = 0.1\text{eV}$), the trivial and topological parts for odd SL no longer cancel out with each other due to the nonzero chemical potential μ and there is a finite total orbital magnetic moment, while for even SL, the magnetic moment behavior is qualitatively similar to that of zero chemical potential case. We also examine more quantitatively the chemical potential μ dependence of the orbital magnetic moment in Fig. S7 at $V_0 = 10\text{meV}$. For even SL, both the trivial part and the topological part are constant in the gap, and when the chemical potential μ is in the conduction bands, there is a rapid change in the orbital magnetic moment due to the contribution from the conduction bands. For odd SL, the topological part varies linearly with μ while the trivial part is constant until the chemical potential reaches the conduction bands, which is consistent with the analytical results in Eq. (S21) and (S22).

The orbital magnetic moments in the thin film model are also calculated, as discussed in the main text. The results are consistent with the two-surface-state model, that $\alpha = 0$ for odd SL and α approaches quantized value $e^2/2h$ in even SL as the sample thickness increases, implying that the two surfaces become less coupled.

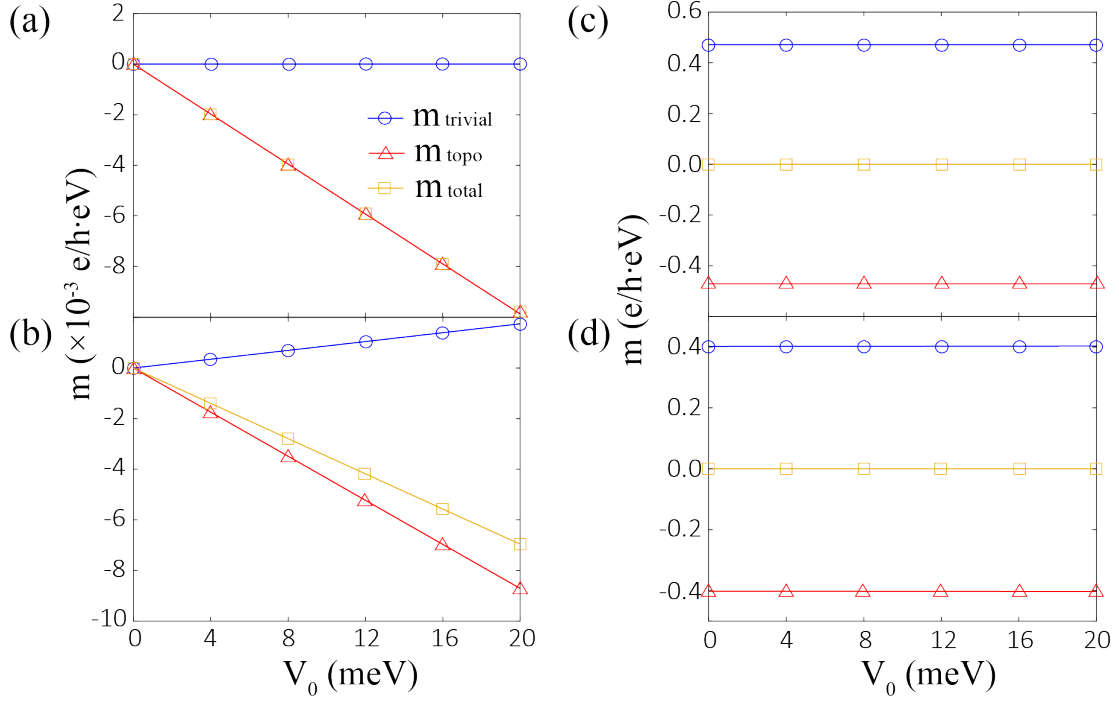


FIG. S5. Orbital magnetic moment density m as a function of asymmetric potential V_0 in the two-surface-state model at $\mu = 0\text{eV}$ and $gM_s = 0.1\text{eV}$ ($g > 0$). (a) AFM1 with $t = 0\text{eV}$. The trivial part remains zero while the topological part increases linearly with V_0 . (b) AFM1 with $t = 0.1\text{eV}$. Both trivial and topological part varies linearly with V_0 but with opposite signs of slopes. (c) Odd SL with $t = 0\text{eV}$. Both trivial and topological part are constant and their sum m_{total} is zero. (d) Odd SL with $t = 0.1\text{eV}$. The trivial and topological part still present zero slopes and cancel out with each other exactly.

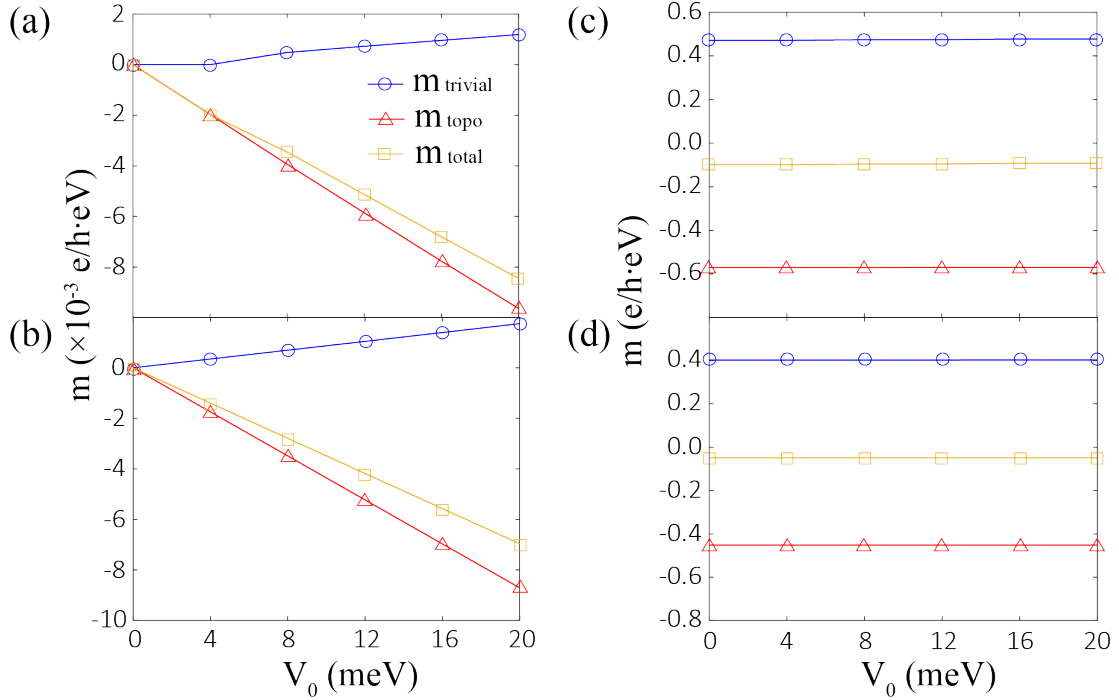


FIG. S6. Orbital magnetic moment density m as a function of asymmetric potential V_0 in the two-surface-state model at $\mu = 0.1\text{eV}$ and $gM_s = 0.1\text{eV}$. (a) AFM1 with $t = 0\text{eV}$. (b) AFM1 with $t = 0.1\text{eV}$. (c) Odd SL with $t = 0\text{eV}$. The total magnetic moment now has nonzero value. (d) Odd SL with $t = 0.1\text{eV}$.

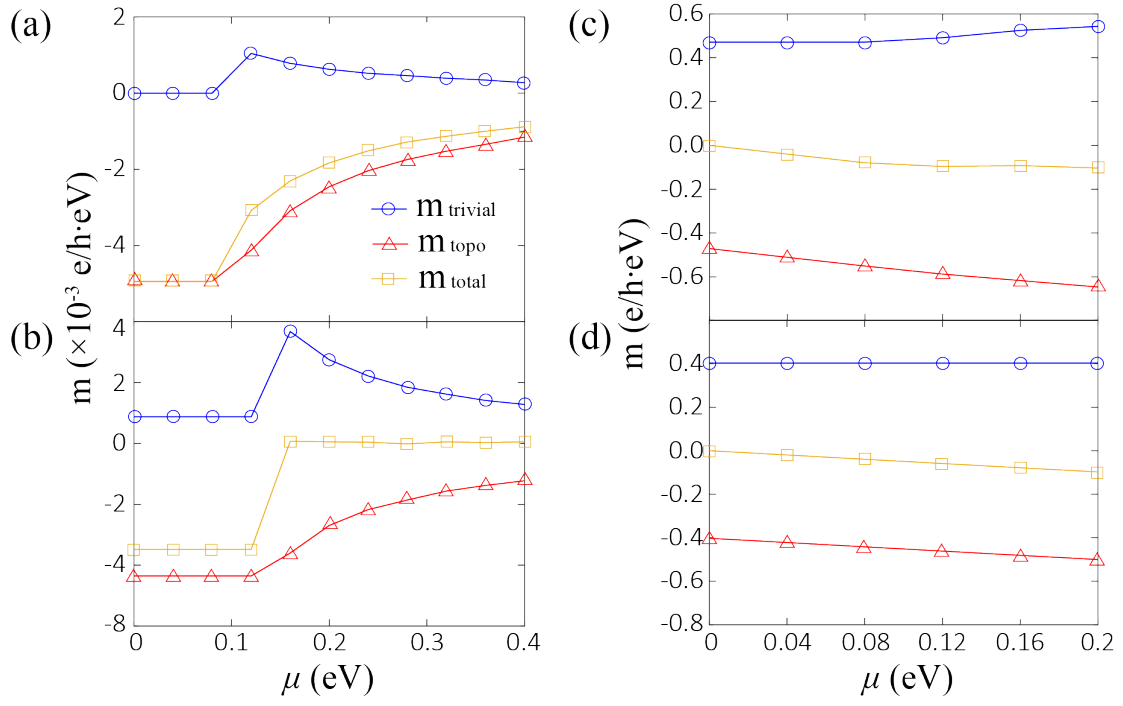


FIG. S7. Orbital magnetic moment density m as a function of chemical potential μ in the two-surface-state model at $V_0 = 10 \text{ meV}$ and $gM_s = 0.1 \text{ eV}$. (a) AFM1 with $t = 0 \text{ eV}$. (b) AFM1 with $t = 0.1 \text{ eV}$. (c) Odd SL with $t = 0 \text{ eV}$. (d) Odd SL with $t = 0.1 \text{ eV}$.